Chapter 3
Ultrashort Pulse Propagation in Nonlinear Dispersive Fibers

Govind P. Agrawal

Abstract This chapter focuses on the evolution of short optical pulses inside optical fibers. After discussing the role of self-phase modulation and optical solitons, we discuss supercontinuum generation, occurring when femtosecond pulses are launched into an optical fiber. The extension of supercontinuum into the mid-infrared and ultraviolet regions is also covered.

Keywords Optical fiber · Group-velocity dispersion · Nonlinear length · Dispersion length · Frequency chirp · Self-phase modulation · Spectral broadening · Optical soliton · Self-steepening · Supercontinuum generation · Soliton fission · Raman scattering · Four-wave mixing · Mid-infrared radiation · Ultraviolet radiation

3.1 Introduction

Ultrashort optical pulses are often propagated through optical waveguides for a variety of applications including telecommunications and supercontinuum generation (Agrawal, 2019). Typically, the waveguide is in the form of an optical fiber, but it can also be a planar waveguide. The material used to make the waveguide is often silica glass, but other materials such as silicon or chalcogenides have also been used in recent years. What is common to all such materials is they exhibit chromatic dispersion as well as the Kerr nonlinearity. The former makes the refractive index frequency-dependent, whereas the latter makes it to depend on the intensity of light propagating through the medium (Maker et al., 1964). Both of these effects become more important as optical pulses become shorter and more intense. For pulses not too short (pulse widths $>$ 1 ns) and not too intense (peak powers $<$ 10 mW), the waveguide plays a passive role (except for small optical losses) and acts as

G. P. Agrawal (✉)
The Institute of Optics, University of Rochester, Rochester, NY, USA
e-mail: gpa@optics.rochester.edu

R. R. Alfano (ed.), *The Supercontinuum Laser Source*,
https://doi.org/10.1007/978-3-031-06197-4_3

a transporter of optical pulses from one place to another, without significantly affecting their shape or spectrum. However, as pulses become shorter and more intense, both the group-velocity dispersion (GVD) and the Kerr nonlinearity start to affect the shape and spectrum of an optical pulse during its propagation inside the waveguide. This chapter focuses on silica fibers, but similar results are expected for other waveguides made of different materials.

Silica fibers have found many interesting applications owing to their nonlinear dispersive nature. They are often used for pulse compression and pulses with durations as short as 6 fs were produced by 1987 (Fork et al., 1987). In the anomalous-GVD regime, fibers support formation of optical solitons, resulting from a balance between the dispersive and nonlinear effects (Hasegawa & Tappert, 1973; Mollenauer et al. 1980; Mollenauer & Stolen, 1984; Stolen 2008). More recently, new types of optical fibers have been developed and used for making a supercontinuum source (Ranka et al. 2000; Dudley et al. 2006; Genty et al. 2007; Dudley & Taylor, 2010). In this case, dispersive effects and several nonlinear phenomena, such as self-phase modulation (SPM), cross-phase modulation (XPM), four-wave mixing (FWM), and stimulated Raman scattering (SRS), work together to produce an extensive spectral broadening of the incident pulse, similar to that observed by Alfano and Shapiro in several 1970 experiments (Alfano & Shapiro, 1970a, 1970b, 1970c, 1971).

This chapter reviews how the nonlinear and dispersive effects in optical fibers influence the propagation of ultrashort pulses with widths in the femtosecond to picosecond range. The basic propagation equation satisfied by the slowly varying amplitude of the pulse envelope is presented in Sect. 3.2. Section 3.3 introduces the dispersive and nonlinear length scales and identifies various propagation regimes of optical pulses. Sections 3.4 and 3.5 then focus separately on the cases of normal- and anomalous-GVD regimes. The phenomenon of supercontinuum generation is studied in Sect. 3.6 in both the normal- and anomalous-GVD regimes of the optical fiber used for this purpose. Extension of the supercontinuum into the ultraviolet (UV) and mid-infrared (mid-IR) regions is covered in Sect. 3.7, as such sources are useful for many practical applications. Section 3.8 provides a summary of the main results and conclusions.

3.2 Basic Propagation Equation

As is the case for all electromagnetic phenomena, we need to solve Maxwell's equations inside a dispersive nonlinear medium. Since details are available elsewhere (Agrawal, 2019), only the main steps are summarized here. Consider the simplest situation in which a single input pulse, polarized linearly at the carrier frequency ω_0, is launched such that it excites a single mode of the fiber. If we assume that the pulse maintains its linear polarization along the x axis during its propagation along fiber's length (the z axis), the electric field can be written in the form

$$\mathbf{E}(\boldsymbol{r}, t) = \frac{1}{2\pi} \int_{-\infty}^{\infty} \hat{x} F(x, y, \omega) \tilde{a}(0, \omega) e^{i[\beta(\omega) z - \omega t]} d\omega, \tag{3.1}$$

where $\hat{x}$ is a unit vector along the x axis and $F(x, y, \omega)$ represents the spatial distribution of the fiber mode. The physical meaning of this equation is clear. Each spectral component of the input field with the amplitude $\tilde{a}(0, \omega)$ acquires a slightly different phase shift because of the frequency dependence of the propagation constant $\beta(\omega)$ associated with that fiber mode.

As an exact functional form of $\beta(\omega)$ is rarely known, it is useful to expand it in a Taylor series around the carrier frequency ω_0 as

$$\beta(\omega) = \beta_0 + (\omega - \omega_0)\beta_1 + \tfrac{1}{2}(\omega - \omega_0)^2 \beta_2 + \cdots, \tag{3.2}$$

where various dispersion parameters are defined as $\beta_m = (d^m \beta / d\omega^m)_{\omega=\omega_0}$. Depending on the pulse bandwidth, one can stop after the group-velocity dispersion (GVD) term containing β_2 or may need to include the third- and higher-order dispersion terms. Another common approximation replaces the mode profile $F(x, y, \omega)$ with its shape at the carrier frequency ω_0. It is also useful to remove the rapidly varying part of the optical field at this frequency and introduce a slowly varying pulse envelope $A(z, t)$ by writing Eq. (3.1) in the form

$$\mathbf{E}(\boldsymbol{r}, t) = \hat{x}\, F(x, y, \omega_0) A(z, t) e^{i(\beta_0 z - \omega_0 t)}. \tag{3.3}$$

Maxwell's equations are then used to derive an equation for $A(z, t)$, representing the slowly varying amplitude of the pulse envelope at distance z.

As outlined in the book by Agrawal (2019), if we include both the Kerr and Raman contributions to the nonlinear susceptibility, the slowly varying pulse envelope $A(z, t)$ satisfies the following time-domain propagation equation:

$$\frac{\partial A}{\partial z} + \frac{\alpha}{2} A = i \sum_{m=1}^{\infty} \frac{i^m \beta_m}{m!} \frac{\partial^m A}{\partial t^m} + i\gamma \left(1 + \frac{i}{\omega_0} \frac{\partial}{\partial t}\right) \times \left(\int_0^{\infty} R(t') |A(z, t - t')|^2 dt' \right) A(z, t), \tag{3.4}$$

where α accounts for fiber losses and the nonlinear parameter γ is defined as

$$\gamma = \frac{\omega_0 n_2(\omega_0)}{c A_{\text{eff}}}, \quad A_{\text{eff}} = \frac{[\iint |F(x, y, \omega_0)|^2 dx dy]^2}{\iint |F(x, y, \omega_0)|^4 dx dy}. \tag{3.5}$$

A_{eff} is known as the effective mode area of the fiber. In the case of supercontinuum generation, it may become necessary to account for the frequency dependence of both $n_2(\omega)$ and $F(x, y, \omega)$.

The nonlinear response function $R(t)$ in Eq. (3.4) includes both the electronic and nuclear (Raman) contributions and can be written as

$$R(t) = (1 - f_R)\delta(t) + f_R h_R(t). \tag{3.6}$$

Both the Raman response function $h_R(t)$ and its fractional contribution ($f_R \approx 0.18$) are known for silica (Stolen et al., 1989). Because of the amorphous nature of silica glasses, the Raman gain spectrum $g_R(\omega)$ of optical fibers, shown in Fig. 3.1a, extends over a frequency range exceeding 50 THz. Since $g_R(\omega)$ is related to the imaginary part of the Fourier transform of $h_R(t)$, it can be used to deduce the real part through the Kramers–Kronig relation. The inverse Fourier transform of $\tilde{h}_R(\omega)$ then provides the Raman response function $h_R(t)$ shown in Fig. 3.1b.

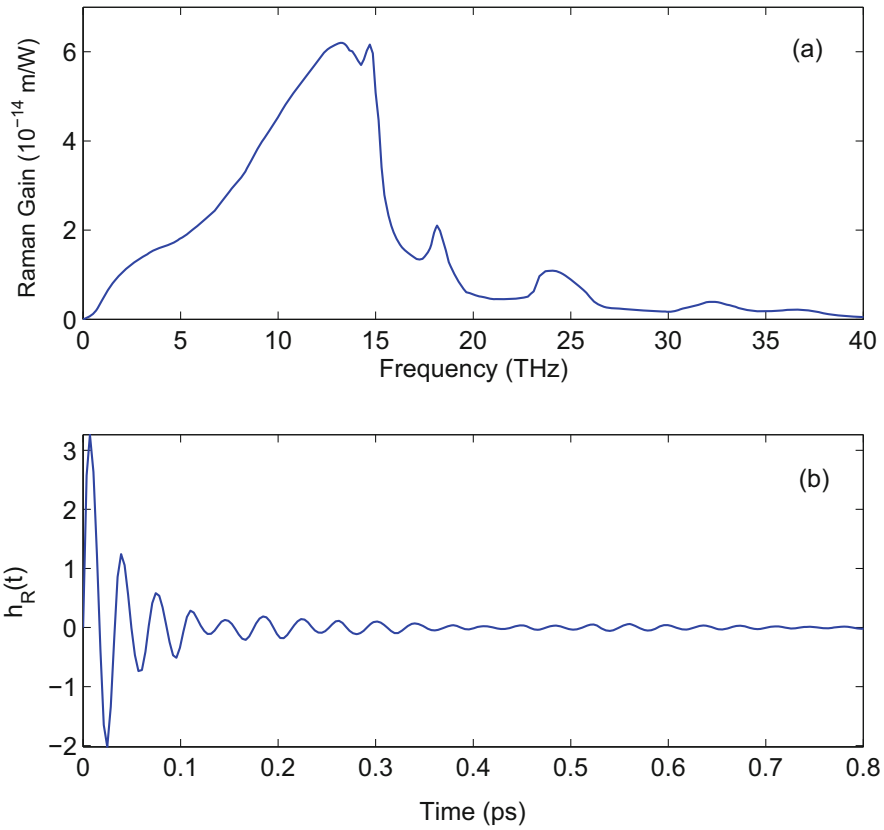

Fig. 3.1 (**a**) Measured Raman gain spectrum of silica fibers (Stolen et al., 1989); (**b**) temporal form of the Raman response function deduced from the gain data

3.3 Different Propagation Regimes

Although Eq. (3.4) must be solved for ultrashort optical pulses, it can be simplified considerably for picosecond pulses, a common situation in many applications. To understand why that is so, we note from Fig. 3.1 that $h_R(t)$ has an appreciable magnitude only for $t < 1$ ps. For pulses wider than 3–4 ps, $h_R(t)$ can be replaced with a delta function $\delta(t)$ with a reasonably good approximation. The derivative term containing ω_0 is also negligible for such pulses. At the same time, all dispersive effects higher than the third order can be ignored for such pulses. Using these three approximations, Eq. (3.4) is reduced to the following simpler equation:

$$\frac{\partial A}{\partial z} + \frac{\alpha}{2}A + \beta_1 \frac{\partial A}{\partial t} + \frac{i\beta_2}{2}\frac{\partial^2 A}{\partial t^2} - \frac{\beta_3}{6}\frac{\partial^2 A}{\partial t^2} = i\gamma |A|^2 A. \tag{3.7}$$

When $\alpha = 0$ and $\beta_3 = 0$, Eq. (3.7) is reduced to the nonlinear Schrödinger (NLS) equation that is well known in the filed of nonlinear optics (Agrawal, 2019). One can justify neglecting the loss term for fibers shorter than 1 km, especially in the wavelength region near 1550 nm where losses are the smallest. However, losses must be included for longer fibers.

Considerable insight can be gained by introducing normalized variables. For this purpose, we note that any input pulse launched into the fiber has its amplitude in the form $A(0, t) = \sqrt{P_0}\, S(t/T_0)$, where $S(t)$ is the shape function, P_0 is the peak power, and T_0 is a measure of the pulse width. For a fiber of length L, it is useful to define the normalized variables as

$$Z = z/L, \qquad \tau = (t - \beta_1 z)/T_0, \qquad A = \sqrt{P_0} e^{-\alpha z/2} U, \tag{3.8}$$

where τ is defined in a frame of reference moving with the pulse at the group velocity $v_g = 1/\beta_1$ (the so-called retarded frame). Note that the exponential decay of the amplitude has been included in the definition of the normalized amplitude U. The use of Eq. (3.8) in Eq. (3.7) leads to an equation in the form

$$\frac{\partial U}{\partial Z} + \frac{isL}{2L_D}\frac{\partial^2 U}{\partial \tau^2} - \frac{\beta_3 L}{6T_0^3}\frac{\partial^3 U}{\partial \tau^3} = \frac{iL}{L_{\mathrm{NL}}} e^{-\alpha z} |U|^2 U, \tag{3.9}$$

where $s = \mathrm{sgn}(\beta_2) = \pm 1$, and the dispersion and nonlinear lengths are defined as

$$L_D = \frac{T_0^2}{|\beta_2|}, \qquad L_{\mathrm{NL}} = \frac{1}{\gamma P_0}. \tag{3.10}$$

They provide two length scales over which the dispersive and nonlinear effects become important for the pulse evolution.

When fiber length L is such that $L \ll L_{\mathrm{NL}}$ and $L \ll L_D$, neither the dispersive nor the nonlinear effects play a significant role during pulse propagation. The fiber

plays a passive role in this regime and acts as a mere transporter of optical pulses (except for reducing the pulse energy because of fiber losses). At a wavelength near 1.5 μm, $\beta_2 \approx -20$ ps^2/km, and $\gamma \approx 2$ W^{-1}km^{-1} for standard telecommunication fibers. The use of these values in Eq. (3.10) shows that the dispersive and nonlinear effects are negligible for $L < 100$ km if $T_0 > 100$ ps and $P_0 < 1$ mW. However, L_D and $L_{\rm NL}$ become smaller as pulses become shorter and more intense. For example, L_D and $L_{\rm NL}$ are ∼0.1 km for $T_0 \sim 1$ ps and $P_0 \sim 1$ W. For such optical pulses, both the dispersive and nonlinear effects need to be included if fiber length exceeds 100 m. Depending on three relative magnitudes of these length scales, the propagation behavior can be classified in the following three regimes.

3.3.1 Dispersion-Dominant Regime

When the fiber length is such that $L \ll L_{\rm NL}$ but $L > L_D$, the last term in Eq. (3.9) is negligible compared to the other two. The dispersion-dominant regime is applicable whenever the fiber and pulse parameters are such that

$$N^2 = \frac{L_D}{L_{\rm NL}} = \frac{\gamma P_0 T_0^2}{|\beta_2|} \ll 1. \tag{3.11}$$

As a rough estimate, P_0 should be less than 10 mW for 10-ps pulses. The parameter N is later found to be related to the soliton order.

In the dispersion-dominant regime, the evolution of an optical pulse is governed by the GVD alone, and the nonlinear effects play a negligible role. The resulting linear equation,

$$\frac{\partial U}{\partial z} + \frac{is}{2L_D}\frac{\partial^2 U}{\partial \tau^2} - \frac{\beta_3}{6T_0^3}\frac{\partial^3 U}{\partial \tau^3} = 0, \tag{3.12}$$

can be solved with the Fourier transform method. Let $\tilde{U}(z, \omega)$ be the Fourier transform of $U(z, \tau)$ defined as

$$\tilde{U}(z, \omega) = \int_{-\infty}^{\infty} U(z, \tau) e^{i\omega\tau}\, d\tau. \tag{3.13}$$

In the Fourier domain, Eq. (3.12) becomes an ordinary differential equation and can be solved easily. Converting the result back to the time domain, we obtain the solution

$$U(z, \tau) = \frac{1}{2\pi}\int_{-\infty}^{\infty} \tilde{U}(0, \omega) \exp\left(\frac{is\omega^2 z}{2L_D} + \frac{i\beta_3\omega^3 z}{6T_0^3} - i\omega\tau\right) d\omega, \tag{3.14}$$

where $\tilde{U}(0, \omega)$ is the Fourier transform of the incident field at $z = 0$ and is obtained by setting $z = 0$ in Eq. (3.13). Equation (3.14) can be used for input pulses of arbitrary shapes. However, the integral can be evaluated in a closed form only for a few specific pulse shapes. In general, both the width and the phase of an optical pulse are expected to change as it propagates down the fiber. It should be stressed, however, that the GVD affects only the spectral phase and not the spectral intensity, i.e., the spectrum of any pulse remains unaltered during its propagation inside a linear dispersive medium.

As a simple example, consider the case of a Gaussian pulse, for which the incident field is of the form $U(0, \tau) = \exp(-\tau^2/2)$, and neglect the contribution of the β_3 term. The integration can be carried out analytically, and the final result is given by

$$U(z, \tau) = \left(1 - is\xi\right)^{-1/2} \exp\left[-\frac{\tau^2}{2(1 - is\xi)}\right], \tag{3.15}$$

where $\xi = z/L_D$ is the distance normalized to the dispersion length. This expression shows that a Gaussian pulse maintains its shape on propagation, but its width T_1 increases with the distance z as

$$T_1(\xi) = T_0(1 + \xi^2)^{1/2}. \tag{3.16}$$

At the same time, the pulse develops a time-dependent phase such that

$$\phi(\xi, \tau) = -\frac{s\xi\tau^2/2}{1 + \xi^2} + \frac{1}{2}\tan^{-1}(s\xi). \tag{3.17}$$

A time-dependent phase implies that the frequency of the electric-field oscillations changes with time, a feature referred to as the frequency chirp. This frequency change is related to the phase as

$$\delta\omega = \omega - \omega_0 = -\frac{\partial\phi}{\partial t} = \frac{s\xi\tau}{(1 + \xi^2)T_0}. \tag{3.18}$$

This relation shows that the frequency changes linearly across the pulse and its value depends on the sign of β_2. In the normal-GVD regime ($s = 1$), $\delta\omega$ is negative near the leading edge and increases linearly across the pulse. The opposite occurs in the anomalous-GVD regime ($s = -1$). As an example, Fig. 3.2 shows dispersion-induced broadening and chirping for a Gaussian pulse at $\xi = 2$ and 4 in the case of anomalous GVD ($s = -1$). As seen there, chirp imposed by GVD is perfectly linear for Gaussian pulses.

One may wonder what happens if the input pulse itself is chirped. In the case of linearly chirped Gaussian pulses, the incident field is of the form $U(0, \tau) = \exp[-(1 + iC)\tau^2/2]$, where C is a chirp parameter. It is common to refer to the chirp as being positive or negative, depending on whether C is positive or negative.

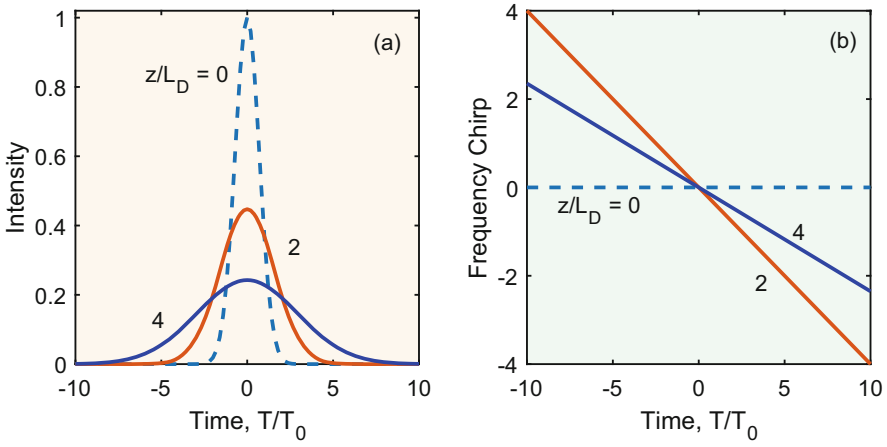

Fig. 3.2 Dispersion-induced broadening (**a**) and chirping (**b**) of a Gaussian pulse at distances of $2L_D$ and $4L_D$ in the case of anomalous GVD ($s = -1$). Dashed lines show the situation at $z = 0$

We can obtain $\tilde{U}(0, \omega)$ from Eq. (3.13) and use it in Eq. (3.14) to find $U(z, \tau)$. The integral can again be done analytically to obtain

$$U(z, \tau) = \frac{1}{\sqrt{Q}} \exp\left[-\frac{(1 + iC)\tau^2}{2Q(z)}\right], \tag{3.19}$$

where $Q = 1 - is\xi(1 + iC)$. Even a chirped Gaussian pulse maintains its shape on propagation, but its width and chirp change as

$$T_1(\xi) = \left[(1 + sC\xi^2)^2 + \xi^2)\right]^{1/2} T_0, \qquad C_1(z) = C + (1 + C^2)s\xi. \tag{3.20}$$

Figure 3.3 shows the broadening factor T_1/T_0 and the chirp parameter C_1 as a function of ξ in the case of anomalous GVD ($s = -1$). An unchirped pulse ($C = 0$) broadens monotonically by a factor of $(1 + \xi^2)^{1/2}$ and develops a negative chirp such that $C_1 = -\xi$ (the dotted curves). Chirped pulses, on the other hand, may broaden or compress depending on whether β_2 and C have the same or opposite signs. When $sC > 0$, a chirped Gaussian pulse broadens monotonically at a rate faster than that of the unchirped pulse (the dashed curves). The situation changes dramatically for $sC < 0$. In this case, the contribution of the dispersion-induced chirp is of a kind opposite to that of the input chirp. As seen from Eq. (3.20), C_1 becomes zero at a distance $\xi = |C|/(1 + C^2)$, and the pulse becomes unchirped. This is the reason why the pulse width initially decreases in Fig. 3.3 and becomes minimum at a specific distance. The minimum value of the pulse width depends on the input chirp parameter as $T_1^{\min} = T_0/\sqrt{1 + C^2}$.

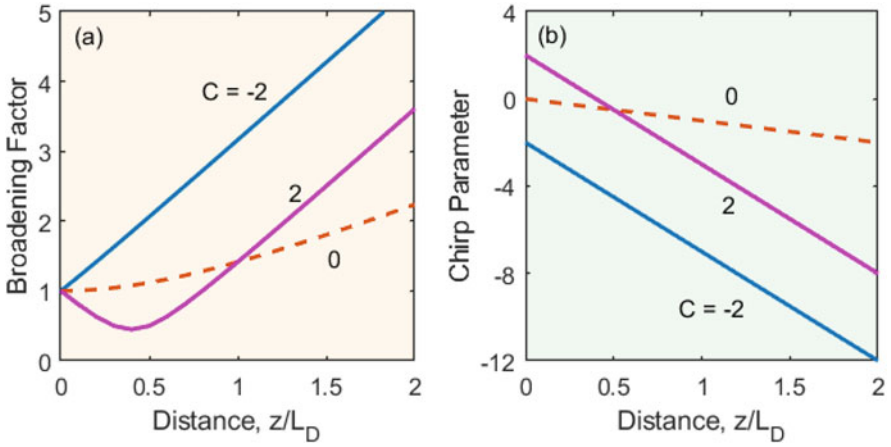

Fig. 3.3 Broadening factor (**a**) and chirp parameter (**b**) for chirped Gaussian input pulses propagating in the anomalous-GVD region of a fiber. Dashed curves show the case of an unchirped Gaussian pulse. The same curves are obtained for normal GVD if the sign of C is reversed

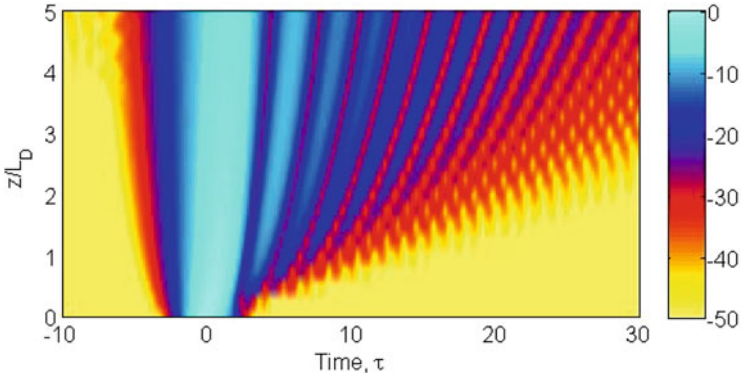

Fig. 3.4 Temporal evolution of an unchirped Gaussian input pulse propagating in the normal-GVD region of a fiber with non-negligible third-order dispersion ($\beta_3/(6T_0^3) = 0.2$)

We briefly consider the impact of third-order dispersion, which becomes important for short pulses propagating near the zero-dispersion wavelength (ZDWL) of the fiber. For a Gaussian input pulse, the integral can be done in a closed form in terms of an Airy function (Agrawal, 2019) but must be performed numerically for other pulse shapes. Figure 3.4 shows the evolution of a Gaussian pulse in the normal-GVD region ($s = 1$) over five dispersion lengths using $\beta_3 L_D/(6T_0^3) = 0.2$. The pulse develops an asymmetric shape with an oscillating structure in its trailing edge. A mirror image around $\tau = 0$ occurs for negative values of β_3 with an oscillating structure developing on the leading edge of the pulse. It will be seen later that the third-order dispersion plays an important role in the formation of a supercontinuum.

3.3.2 Nonlinearity-Dominant Regime

When the fiber length L is such that $L \ll L_D$ but $L > L_{\rm NL}$, the dispersion terms in Eq. (3.9) are negligible compared to the nonlinear term. In that case, pulse evolution in the fiber is governed by the SPM alone, which produces changes in the pulse spectrum but leaves the pulse shape intact. The nonlinearity-dominant regime is applicable only when $N \gg 1$. If we neglect the dispersion terms in Eq. (3.9), it can be solved analytically to obtain the general solution

$$U(L,\tau) = U(0,\tau)\exp[i\phi_{\rm NL}(L,\tau)], \tag{3.21}$$

where $\phi_{\rm NL}(L,\tau) = |U(0,\tau)|^2(L_{\rm eff}/L_{\rm NL})$. The effective length $L_{\rm eff}$ for a fiber of length L is defined as $L_{\rm eff} = [1-\exp(-\alpha L)]/\alpha$. It is smaller than L because of fiber losses. In the absence of fiber losses, $L_{\rm eff} = L$. Equation (3.21) shows that SPM gives rise to an intensity-dependent phase shift, but the pulse shape remains unaffected. The maximum phase shift $\phi_{\rm max}$ occurs at the pulse center located at $\tau = 0$. With U normalized such that $|U(0,0)| = 1$, it is given by

$$\phi_{\rm max} = L_{\rm eff}/L_{\rm NL} = \gamma P_0 L_{\rm eff}. \tag{3.22}$$

If we use $\gamma = 2\,{\rm W}^{-1}/{\rm km}$ and $L_{\rm eff} = 20\,{\rm km}$, $\phi_{\rm max} = 40$ at a power level $P_0 = 1\,{\rm W}$.

Spectral changes induced by SPM are a direct consequence of the time dependence of $\phi_{\rm NL}$. Recalling that a temporally varying phase implies that the pulse becomes chirped such that

$$\delta\omega(\tau) = -\frac{\partial\phi_{\rm NL}}{\partial t} = -\left(\frac{L_{\rm eff}}{L_{\rm NL}}\right)\frac{1}{T_0}\frac{\partial}{\partial\tau}|U(0,\tau)|^2. \tag{3.23}$$

The chirp induced by SPM increases in magnitude with the propagated distance. In other words, new frequency components are generated continuously as the pulse propagates down the fiber. These SPM-generated frequency components broaden the spectrum compared to its initial width at $z = 0$. The spectrum is obtained by taking the Fourier transform of Eq. (3.21). Figure 3.5 shows the spectrum $|\tilde{U}(L,\omega)|^2$ calculated for an unchirped Gaussian pulse using $\phi_{\rm max} = 40$. In this situation, the number of internal peaks increases linearly with the fiber length, and the dominant peaks occur near the spectral boundaries. These SPM-induced spectral features were first observed in optical fibers in a 1978 experiment (Stolen & Lin, 1978) and were used to estimate the nonlinear parameter n_2.

Since the nonlinear phase $\phi_{\rm NL}$ depends on the pulse intensity, its derivative needed in Eq. (3.23) is quite sensitive to the shape of the pulse. This feature makes the SPM-broadened spectrum to depend on the pulse shape. We can see this dependence by considering super-Gaussian pulses whose intensity varies with time as $|U(0,\tau)|^2 = \exp(-\tau^{2m})$, where $m > 1$ for super-Gaussian pulses. The pulse becomes nearly rectangular for $m > 5$. Figure 3.6 compares the evolution of

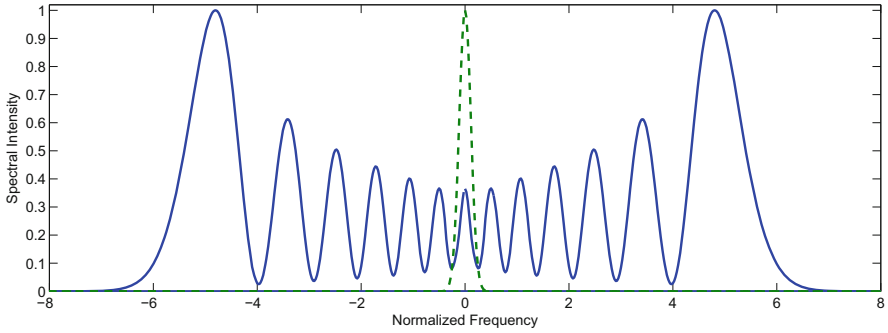

Fig. 3.5 SPM-induced spectral broadening of a Gaussian pulse for $\phi_{\max} = 40$. The dashed curve shows the input spectrum

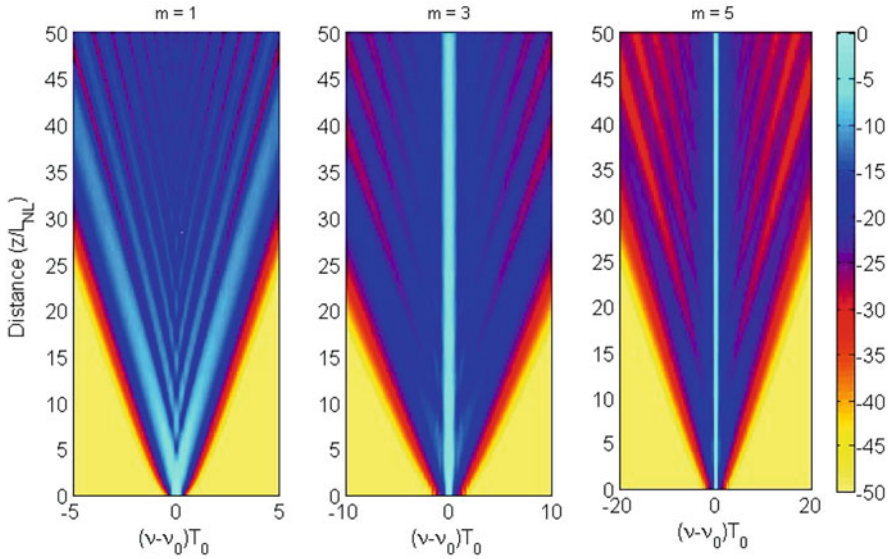

Fig. 3.6 Evolution of SPM-broadened spectra for fiber lengths in the range 0 to $50L_{\mathrm{NL}}$ for unchirped super-Gaussian pulses with $m = 1$, 3, and 5. A color bar shows the 50-dB range used for plotting the spectral density

pulse spectra for the Gaussian ($m = 1$) and super-Gaussian ($m = 3$ and 5) pulses over $50\,L_{\mathrm{NL}}$ using Eq. (3.22) in Eq. (3.21) and performing the Fourier transform numerically. In all cases, input pulses are assumed to be unchirped ($C = 0$), and fiber losses are ignored ($\alpha = 0$). The qualitative differences between the three spectra are quite noticeable. Even though all spectra in Fig. 3.6 exhibit multiple peaks, most of the energy remains in the central peak for a super-Gaussian pulse. This is so because the chirp is nearly zero over the central region for such a pulse, a consequence of the nearly uniform intensity of super-Gaussian pulses for

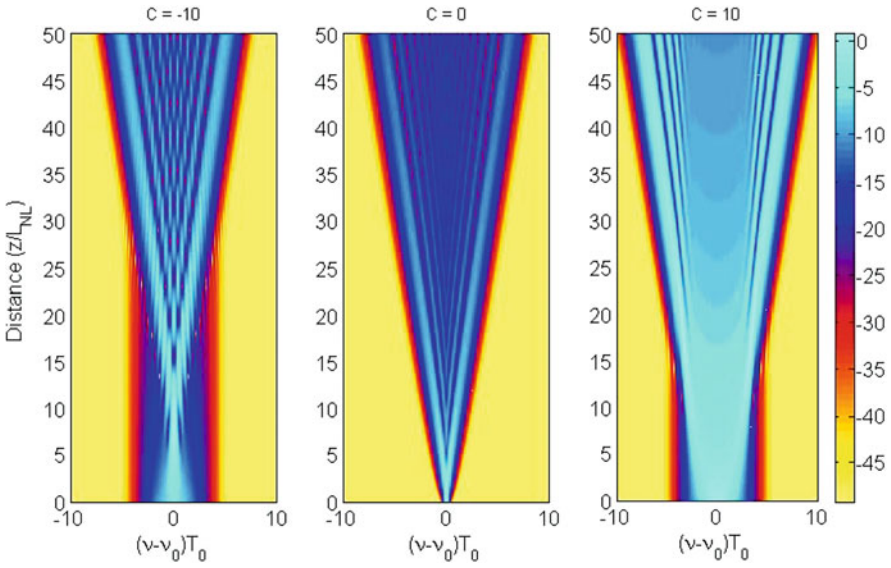

Fig. 3.7 Evolution of SPM-broadened spectra for fiber lengths in the range 0 to $50L_{\rm NL}$ for chirped Gaussian pulses with $C = -10$, 0, and 10. A color bar shows the 50-dB range used for plotting the spectral density

$|t| < T_0$. In contrast, most of the energy appears in the outermost spectral peaks for a Gaussian pulse. The spectral range becomes larger for super-Gaussian pulses because the maximum chirp becomes larger as m increases. A triangular shape of the spectral evolution in Fig. 3.6 indicates that the SPM-induced spectral broadening increases linearly with distance.

An initial frequency chirp on the input pulse can also lead to drastic changes in the SPM-broadened pulse spectrum. This is illustrated in Fig. 3.7, which compares the spectral evolution of a Gaussian pulse for $C = -10$, 0, and 10 under conditions identical to those used in Fig. 3.6. It is evident that the sign of the chirp parameter C plays a critical role. For $C > 0$, spectral broadening increases, and the oscillatory structure becomes less pronounced. However, a negatively chirped pulse undergoes a spectral narrowing phase before its spectrum begins to broaden and exhibit multiple peaks. This behavior can be understood from Eq. (3.23) by noting that the SPM-induced chirp is linear and positive (frequency increases with increasing time) over the central portion of a Gaussian pulse. Thus, it adds to the initial chirp for $C > 0$, resulting in a broader spectrum. In the case of $C < 0$, the two chirp contributions are of opposite signs (except near the pulse edges), and the pulse becomes less chirped. If we employ the approximation that $\phi_{\rm NL}(t) \approx \phi_{\max}(1 - t^2/T_0^2)$ near the pulse center for Gaussian pulses, the SPM-induced chirp is nearly canceled for $C = -2\phi_{\max}$. This relation provides a rough estimate of the distance at which which narrowest spectrum occurs for a given value of C.

3.3.3 Dispersive Nonlinear Regime

When the fiber length L is longer or comparable to both L_D and L_{NL}, dispersion and nonlinearity act together as the pulse propagates along the fiber. The interplay of the GVD and SPM effects can lead to a qualitatively different behavior compared with that expected from GVD or SPM alone. In the anomalous-GVD regime ($\beta_2 < 0$), the fiber can support solitons. Equation (3.9) is helpful in understanding pulse evolution in optical fibers when both the dispersive and nonlinear effects should be taken into account. It is a fundamental equation of nonlinear science and has been studied extensively in many different contexts. The β_3 term is often negligible in practice. The parameter β_2 can be positive or negative with values in the range 0.1–20 ps^2/km, depending on how close the pulse wavelength is to the ZDWL of the fiber. The nonlinear parameter γ is positive and has a value in the range of 1–10 W^{-1}/km for most silica fibers; its values can be increased to beyond 100 W^{-1}/km in narrow-core photonic crystal fibers; even values >1000 W^{-1}/km have been realized using non-silica glasses.

It is useful to normalize the distance as $\xi = z/L_D$ and write Eq. (3.9) in the form (assuming that the β_3 term is negligible)

$$\frac{\partial U}{\partial \xi} + \frac{is}{2}\frac{\partial^2 U}{\partial \tau^2} = N^2 e^{-\alpha z}|U|^2 U. \tag{3.24}$$

In the lossless case ($\alpha = 0$), Eq. (3.24) becomes the standard NLS equation. Its solutions depend on the nature of dispersion through $s = \pm 1$ and on the peak power of the input pulse through the parameter N. They also depend on the pulse shape. As an example, Fig. 3.8 shows the temporal and spectral evolution of an initially unchirped Gaussian-shape pulse launched in the anomalous-GVD regime ($s = -1$) with a peak power such that $N = 1$. The pulse broadens slightly, and its spectrum narrows a bit, but neither the temporal nor the spectral width of the pulse changes much after a dispersion length. The pulse also appears to lose some energy in the form of dispersive waves that form a low-intensity pedestal around the pulse.

This behavior can be understood by noting that the NLS equations have exact solutions in the form of solitons in the case of anomalous GVD. For an initial pulse shape $U(0, \tau) = \mathrm{sech}(\tau)$ and integer values of the parameter N, the solitons follow a periodic evolution pattern with the period $\xi_0 = \pi/2$. The fundamental soliton corresponds to $N = 1$ and propagates without change in its shape. The only reason that the pulse shape and spectrum change in Fig. 3.8 is that the initial pulse shape is Gaussian and does not correspond to a soliton. Indeed, if we repeat the calculation with a "sech" pulse shape, we find that both the shape and spectrum do not change with z. From Eq. (3.11), the peak power necessary to excite the fundamental soliton is given by $P_1 = |\beta_2|/\gamma T_0^2$. For a hyperbolic secant pulse, the pulse width is related to T_0 by $T_p \approx 1.76 T_0$. This relation should be used for comparison with experiments. As a rough estimate, for 1.55 μm solitons to form in silica fibers, $P_1 \sim 1$ W when $T_p = 1$ ps. In the next two sections, we consider the

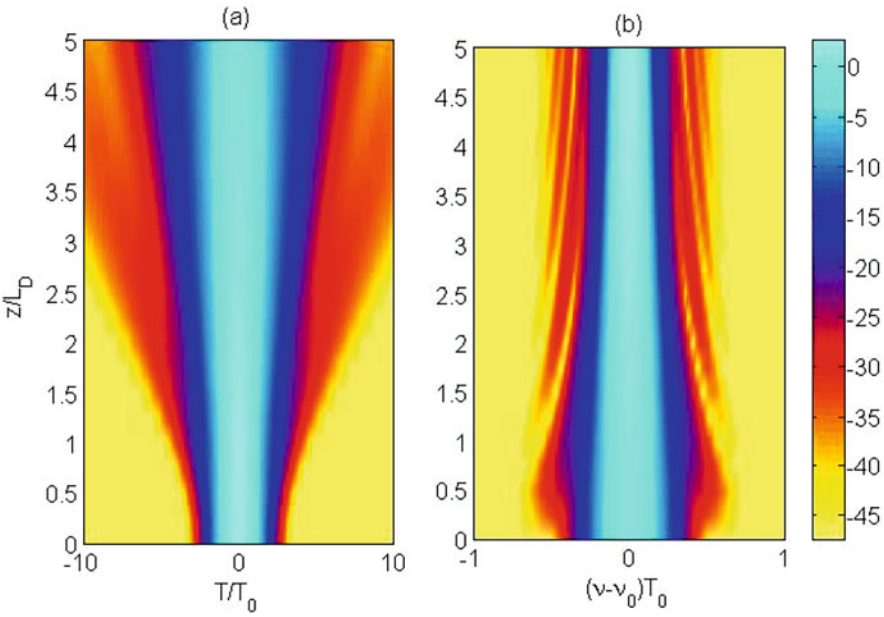

Fig. 3.8 Temporal and spectral evolution of an initially Gaussian-shape pulse launched in the anomalous-GVD region with a peak power such that $N = 1$. The color bar shows 50-dB range used for plotting the intensity

pulse propagation in the normal and anomalous GVD regimes by solving Eq. (3.24) numerically with the split-step Fourier method (Agrawal, 2019).

3.4 Normal Dispersion

In the normal-GVD region, the GVD parameter $\beta_2 > 0$ and $s = 1$ in Eq. (3.24). We set $\alpha = 0$ assuming that the fiber is short enough that losses are negligible. The parameter N can vary over a wide range depending on the widths and peak powers of input pulses. As an example, Fig. 3.9 shows the evolution of pulse shape and spectrum over one dispersion length for a sech-shape pulse launched with $N = 5$. Initially, the spectrum broadens because of SPM-induced chirping, while pulse shape remains almost unchanged. However, spectral broadening saturates at a distance of about $\xi = 0.3$, and beyond that the chirped pulse starts to broaden, and its shape changes drastically with a nearly flat central region.

An interesting phenomenon occurs for larger values of N. Figure 3.10 shows the evolution of an initially sech-shape pulse launched such that $N = 30$. As the pulse propagates, it broadens and develops a nearly rectangular profile with sharp leading and trailing edges. The combination of rapidly varying intensity and SPM in

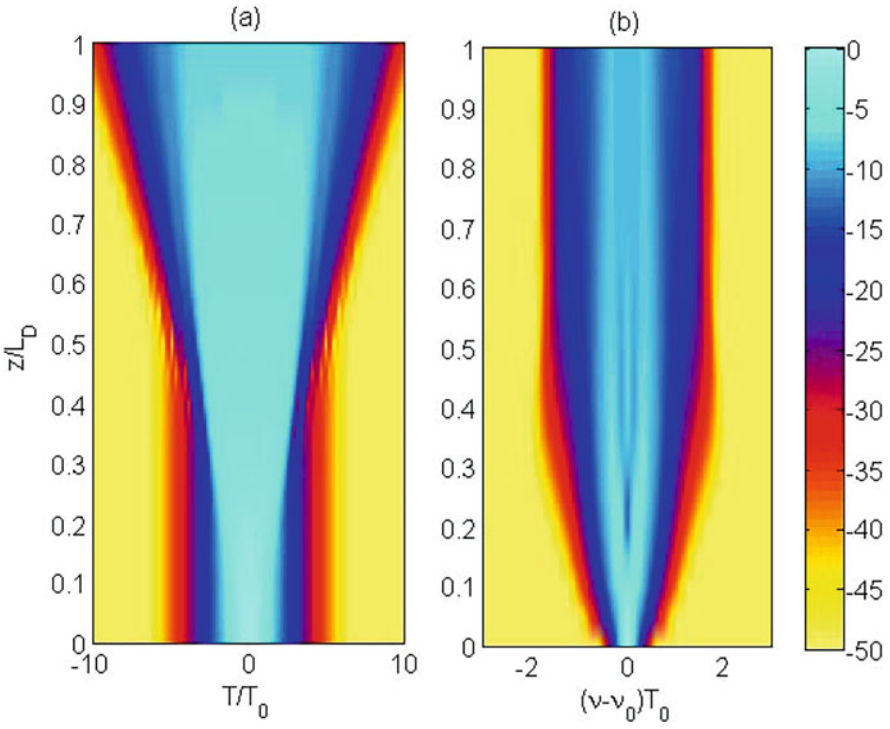

Fig. 3.9 Evolution of (**a**) pulse shape and (**b**) spectrum over one dispersion length in the normal-GVD region when a sech-shape pulse is launched with $N = 5$

these steep-slope regions broadens the pulse spectrum. Because the new frequency components are mainly generated near the edges, the pulse develops a nearly linear frequency chirp across its entire width. This linear chirp can be used to compress the pulse by passing it subsequently through a dispersive delay line such as a grating pair (Agrawal, 2020).

An interesting feature of Fig. 3.10 is the presence of rapid oscillations in the wings of the pulse. These can be more clearly in Fig. 3.11 where the pulse and spectrum are plotted at $\xi = 0.1$. In a 1985 paper, Tomlinson et al. (1985) interpreted such oscillations in terms of optical wave breaking, resulting from a mixing of the SPM-induced frequency-shifted components with the unshifted light in the wings. This phenomenon can also be understood as a FWM process. Indeed, one can clearly see two side bands in the pulse spectrum, as expected for a FWM process. The central structure in the spectrum is due to SPM (see Fig. 3.5). The results shown in Figs. 3.10 and 3.11 are for an initially unchirped pulse. If input pulses are chirped, they may follow a different evolution pattern than that shown in Fig. 3.10.

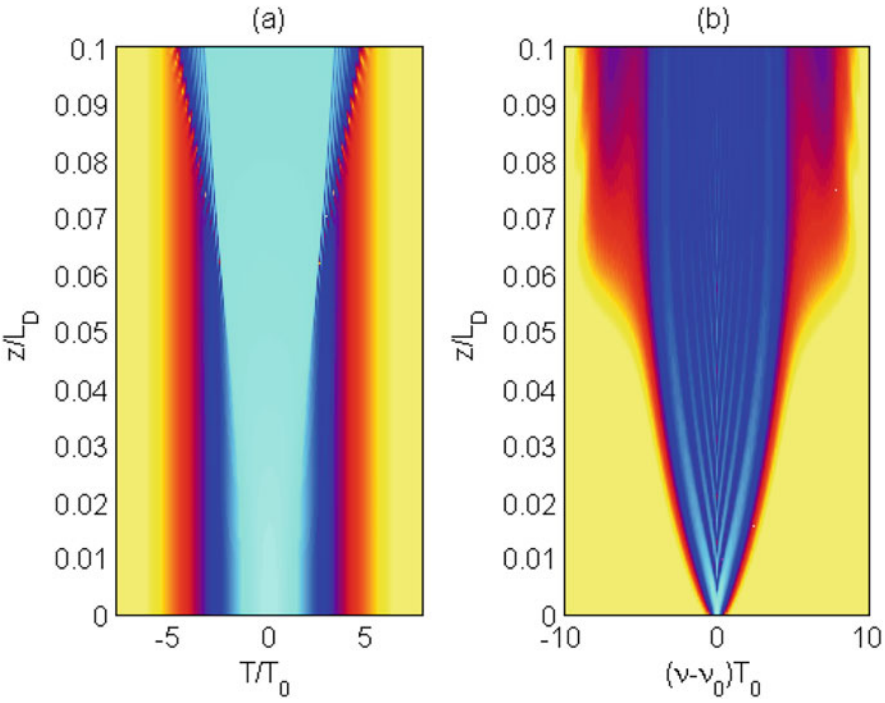

Fig. 3.10 Same as Fig. 3.9 except that the pulse is launched with $N = 30$. The color schemes are also identical in two figures

3.5 Anomalous Dispersion

In the anomalous-GVD regime, the GVD parameter $\beta_2 < 0$ and $s = -1$ in Eq. (3.24). For silica fibers, this is typically the situation in the spectral region near 1.55 μm that is of considerable interest for telecommunications. As mentioned earlier, a simple sign change leads to the formation of optical solitons. In particular, a sech-shape input pulse launched with $N = 1$ forms a fundamental soliton and propagates without any change in its shape. In the absence of fiber losses, the fundamental solitons can propagate undistorted for arbitrarily long distances (Hasegawa & Tappert, 1973). The soliton formation capacity of optical fibers has led to the development of the soliton laser (Mollenauer & Stolen, 1984). A piece of single-mode fiber inside the cavity was used to shape the intra-activity pulses, and the width of output pulses was controlled by adjusting the fiber length. Pulses as short as 50 fs have been generated directly from a soliton laser.

All higher-order solitons ($N > 1$) follow a periodic evolution pattern along the fiber with a period $z_0 = (\pi/2)L_D$. Figure 3.12 shows, as an example, the evolution pattern of the $N = 3$ soliton over one period, obtained by solving Eq. (3.24) with $U(0, \tau) = \text{sech}(t)$. The pulse initially narrows, develops a two-peak structure, and

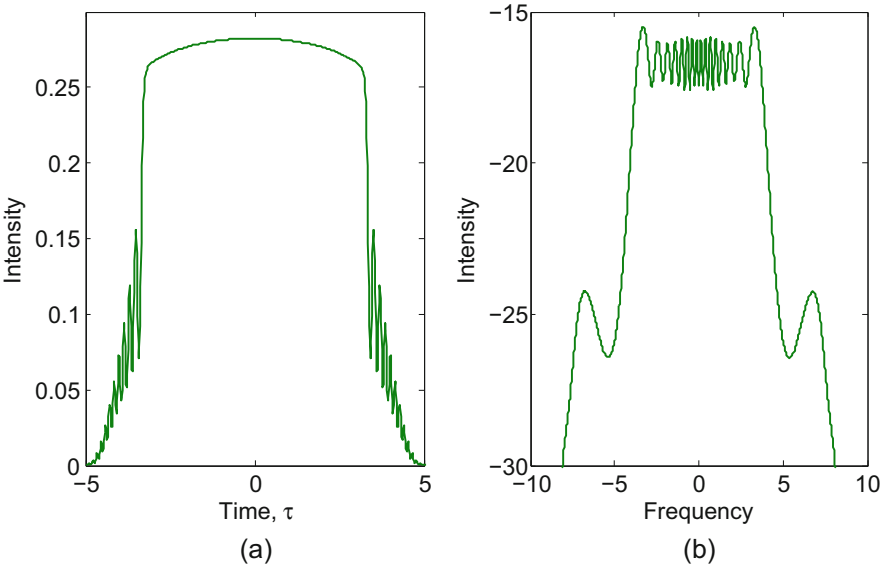

Fig. 3.11 (**a**) Pulse shape and (**b**) spectrum at $\xi = 0.1$ for $N = 30$. Two sidebands in the spectrum and temporal oscillations near the pulse edges are due to optical wave breaking

then reverses its propagation behavior beyond $z/L_D = \pi/4$ such that the original pulse is restored at $z/L_D = \pi/2$. Initial narrowing of the higher-order soliton can used to compress an optical pulse by suitably selecting its peak power and the fiber length (Agrawal, 2020).

3.5.1 Fission of High-Order Solitons

Equation (3.24) has proved to be very useful in understanding the propagation behavior in the anomalous-GVD regime of optical fibers. However, as discussed in Sect. 3.2, the NLS equation is not adequate for ultrashort pulses ($T_0 < 1$ ps), and its generalized version, Eq. (3.4), should be used in its place. It turns out that even the inclusion of third-order dispersion (TOD) affects the soliton dynamics considerably. As an example, Fig. 3.13 shows the evolution under conditions identical to those of Fig. 3.12 except that the TOD is included using $\delta_3 = \beta_3 L_D/6T_0^3 = 0.02$. The propagation distance was increased to $3L_D$ to identify all new features clearly. The TOD breaks up the third-order soliton into three fundamental solitons of different widths and peak powers, a phenomenon called soliton fission (Wai et al., 1986). A clear evidence of soliton fission is seen in the spectral evolution, where we see a sudden emergence of a new spectral peak at a distance of about $z = 0.4L_D$ on the high-frequency (blue) side of the pulse spectrum. This peak represents a dispersive

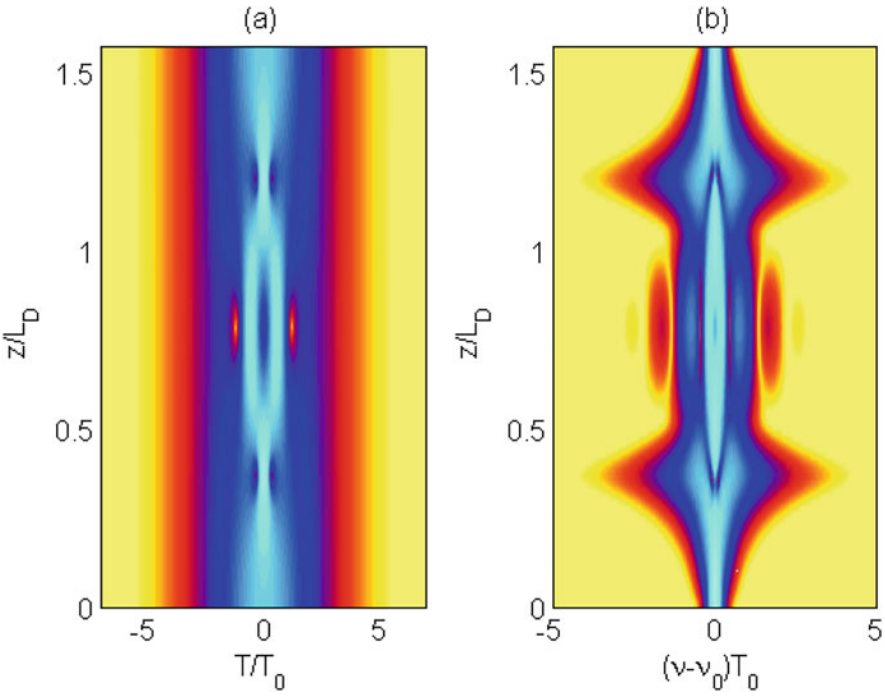

Fig. 3.12 Evolution of a third-order soliton from $\xi = 0$ to $\pi/2$; (**a**) pulse shape and (**b**) spectrum. The color bar is identical to that in Fig. 3.9

wave created after the fission through a Cherenkov-like phase-matching process (Akhmediev & Karlsson, 1995).

To understand the physics behind soliton fission, we need to realize that a high-order soliton, say of the order N, actually consists of N fundamental solitons that evolve, in the absence of TOD, as one entity in a periodic fashion because they move at the same speed inside the fiber. However, their speeds become slightly different when the TOD is not negligible. This feature destroys their periodic evolution, and individual fundamental solitons separate from each other as they travel inside the fiber. The inverse scattering method shows that the widths and peak powers of the individual fundamental solitons are related to the width T_0 and peak power P_0 of the input pulse as (Kodama & Hasegawa, 1987)

$$T_k = \frac{T_0}{2N+1-2k}, \qquad P_k = \frac{(2N+1-2k)^2}{N^2} P_0, \tag{3.25}$$

where k varies from 1 to N.

The TOD affects the dynamics of each fundamental soliton after the soliton fission because solitons can propagate unperturbed only in its absence. The TOD-induced perturbation forces each soliton to shed some energy in the form of a

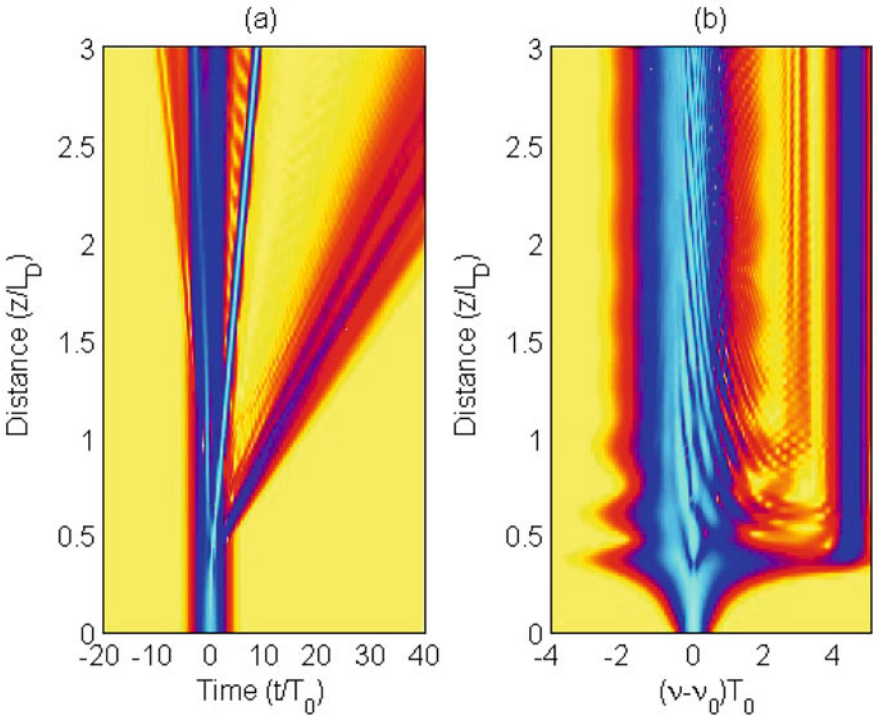

Fig. 3.13 Fission of a third-order soliton induced by TOD ($\delta_3 = 0.02$); (**a**) pulse shape (red tilted cone) and (**b**) spectrum (vertical blue line) show the signature of a blue-shifted dispersive wave. The color scheme is identical to that in Fig. 3.9

dispersive wave. Generation of dispersive waves through TOD attracted considerable attraction soon after this phenomenon was identified numerically (Wai et al., 1990; Gordon, 1992; Roy, 2009). Such radiation is also known as the Cherenkov radiation (Akhmediev & Karlsson, 1995). It is emitted at a frequency at which phase velocity of the dispersive wave matches that of the soliton. The frequency shift between the soliton and the dispersive wave is the temporal analog of the angle at which the Cherenkov radiation is emitted by charged particles in a bulk medium.

The frequency of the dispersive wave that grows because of radiation emitted by the perturbed soliton can be obtained by a simple phase-matching argument requiring that the dispersive wave at frequency ω propagates with the same phase velocity as that of the soliton at the frequency ω_s. The frequency shift $\Omega = \omega - \omega_s$ is found by the roots of a third-order polynomial (Akhmediev & Karlsson, 1995)

$$\beta_2 \Omega^2 + \frac{\beta_3}{3} \Omega^3 - \gamma P_s = 0, \tag{3.26}$$

where P_s is the peak power of the fundamental soliton formed after the fission process (and not that of the input pulse). Similarly, the dispersion parameters appearing in Eq. (3.26) are at the soliton central frequency ω_s. The only real solution of this polynomial is approximately given by

$$\Omega \approx -\frac{3\beta_2}{\beta_3} + \frac{\gamma P_s \beta_3}{3\beta_2^2}. \tag{3.27}$$

For solitons propagating in the anomalous-GVD region such that $\beta_2 < 0$ and $\beta_3 > 0$, the frequency shift of the dispersive wave is positive. As a result, the dispersive wave is emitted at a higher frequency (a blue shift) than that of the soliton. This was the case for the numerical results shown in Fig. 3.13. Indeed, the dispersive-wave frequency seen in this figure agrees well with the prediction of Eq. (3.27).

3.5.2 Intrapulse Raman Scattering

The Raman term appearing in Eq. (3.4) affects the fission process considerably through a phenomenon known as the soliton self-frequency shift. First observed in 1986, it manifests as a red shift of short optical pulses propagating as fundamental solitons (Mitschke & Mollenauer, 1986). Physically, the low-frequency components of the pulse are amplified from the Raman gain by the high-frequency components of the same pulse (Gordon, 1986). Since such an amplification is not restricted to solitons, the term Raman-induced frequency shift (RIFS) or intrapulse Raman scattering is also employed (Santhanam & Agrawal, 2003). Large values of the RIFS (>50 THz) were observed after 2000 with the advent of microstructured fibers (Liu et al., 2001).

In a 1987 experiment, 30-fs input pulses of different peak powers (resulting in different values of N) were launched into a 1-km-long fiber, and their spectra observed at its output end (Beaud et al., 1987). The fission process occurred at different distances within the fiber for different N values, but in all cases the spectrum of each fundamental soliton shifted toward longer wavelengths because of intrapulse Raman scattering, the shortest pulse exhibiting the largest shift. At the highest peak power of 530 W, three distinct spectral peaks appeared that corresponded to three fundamental solitons. The shortest soliton had a RIFS of nearly 200 nm.

For the sake of comparison, Fig. 3.14 shows the evolution of a third-order soliton under conditions identical to those of Fig. 3.13 except that, in addition to the TOD, intrapulse Raman scattering is also included by solving Eq. (3.4) numerically. In addition to the blue-shifted dispersive wave (appearing as a red cone on the left), one can see a considerable red shift of the shortest soliton that increases continuously with distance. In the time domain, this red shift leads to bending of the soliton trajectory because of a continuous slowing down of the red-shifted soliton owing to changes in its group velocity. It should be clear by now that the generalized

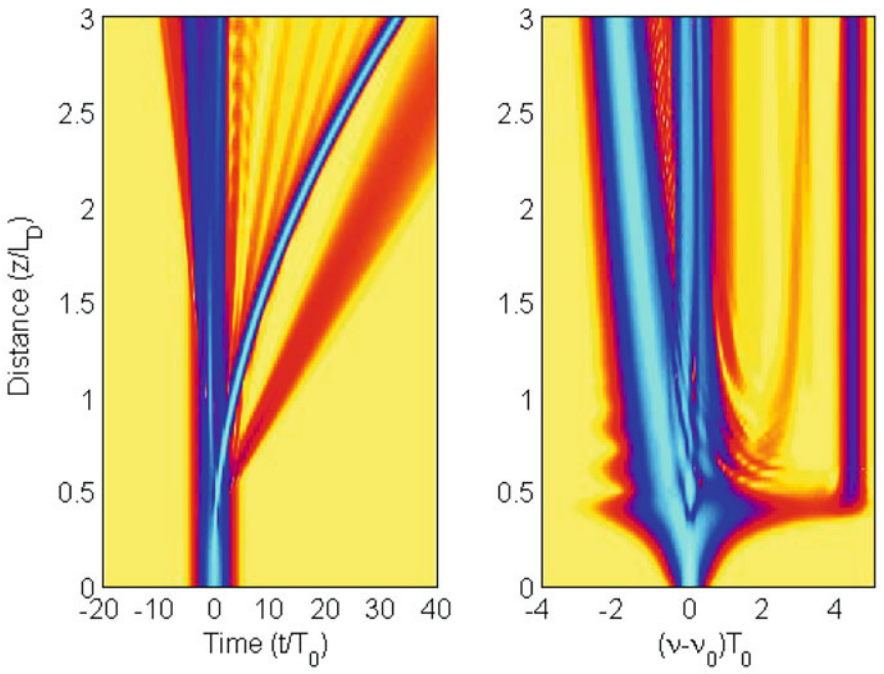

Fig. 3.14 Fission of a third-order soliton in the presence of TOD ($\delta_3 = 0.02$) and intrapulse Raman scattering. In addition to a blue-shifted dispersive wave, the shortest soliton slows down (light blue curve on the left). The color scheme is identical to that in Fig. 3.9

NLS equation, Eq. (3.4), should be used for a realistic description of the underlying physics when ultrashort pulses are propagated through optical fibers.

3.6 Supercontinuum Generation

As we saw in Sect. 3.5, when an optical pulse propagates through a nonlinear dispersive fiber, its temporal as well as spectral evolution is affected not only by a multitude of nonlinear effects but also by the dispersive properties of that fiber. It turns out that, for sufficiently intense pulses, the pulse spectrum becomes so broad that it often extends over a frequency range exceeding 50 THz. Such extreme spectral broadening is referred to as *supercontinuum generation*, a phenomenon first observed around 1970 in a glassy bulk nonlinear medium (Alfano & Shapiro, 1970a). In the context of optical fibers, a supercontinuum was first observed in 1976 using 10-ns pulses from a dye laser (Lin & Stolen, 1976). Although this topic attracted some attention during the decades of 1980s and 1990s, it was only after 2000, with the emergence of microstructured and photonic crystal fibers (PCFs), that

the use of optical fibers for supercontinuum generation became common (Dudley et al. 2006; Genty et al. 2007; Dudley & Taylor, 2010).

In a 2000 experiment, 100-fs pulses with 7-kW peak power at 790 nm were launched in the anomalous-GVD region of a microstructured fiber that was only 75 cm long (Ranka et al., 2000). Even for such a short fiber, the supercontinuum extended from 400 to 1600 nm; it was also relatively flat over the entire bandwidth (on a logarithmic power scale). Since then, similar features have been observed in many experiments using different types of fibers. In this section, we review the physical mechanisms behind the supercontinuum generation using optical fibers and discuss the progress realized since the year 2000.

3.6.1 Supercontinuum Generation Through Soliton Fission

The important question is what physical processes within an optical fiber are responsible for generating such a wide supercontinuum. The answer turned out to be the soliton fission in the case of femtosecond pulses. One can see a hint of this in Fig. 3.14 showing the evolution of a third-order soliton over three dispersion lengths. The pulse spectrum at $z = 3L_D$ has broadened considerably compared to its input shape and consists of multiple peaks. In addition to the central SPM-broadened structure and the leftmost dominant peak that corresponds to the shortest soliton created after the soliton fission, there is blue-shifted peak on the right belonging to a dispersive wave. Moreover, several other peaks have begun to appear as a result of XPM and FWM. The spectrum in Fig. 3.14 cannot yet be called a supercontinuum, but it is not difficult to imagine that a supercontinuum may form for solitons of much higher orders.

As an example, Fig. 3.15 shows the evolution of an eighth-order soliton ($N = 8$) over one dispersion length, obtained by solving Eq. (3.4) numerically in its following dimensionless form:

$$i\frac{\partial U}{\partial \xi} - \frac{s}{2}\frac{\partial^2 U}{\partial \tau^2} - i\delta_3\frac{\partial^3 U}{\partial \tau^3} + \delta_4\frac{\partial^4 U}{\partial \tau^4} = N^2\left(1 + if_s\frac{\partial}{\partial \tau}\right)\left(U(\xi,\tau)\int_0^\infty R(\tau')|U(\xi,\tau-\tau')|^2 d\tau'\right), \quad (3.28)$$

where $s = \pm 1$ and $f_s = (\omega_0 T_0)^{-1}$ is the self-steepening parameter. We have retained dispersion up to fourth order through

$$\delta_3 = \beta_3 L_D/(6T_0^3), \qquad \delta_4 = \beta_4 L_D/(24T_0^4). \quad (3.29)$$

In obtaining Fig. 3.15, we used $U(0,t) = \mathrm{sech}(t/T_0)$ with $T_0 = 50$ fs, neglected the self-steepening term by setting $f_s = 0$, and used the form of $h_R(t)$ suggested by Lin and Agrawal in a 2006 paper (Lin & Agrawal, 2006). The two dispersion

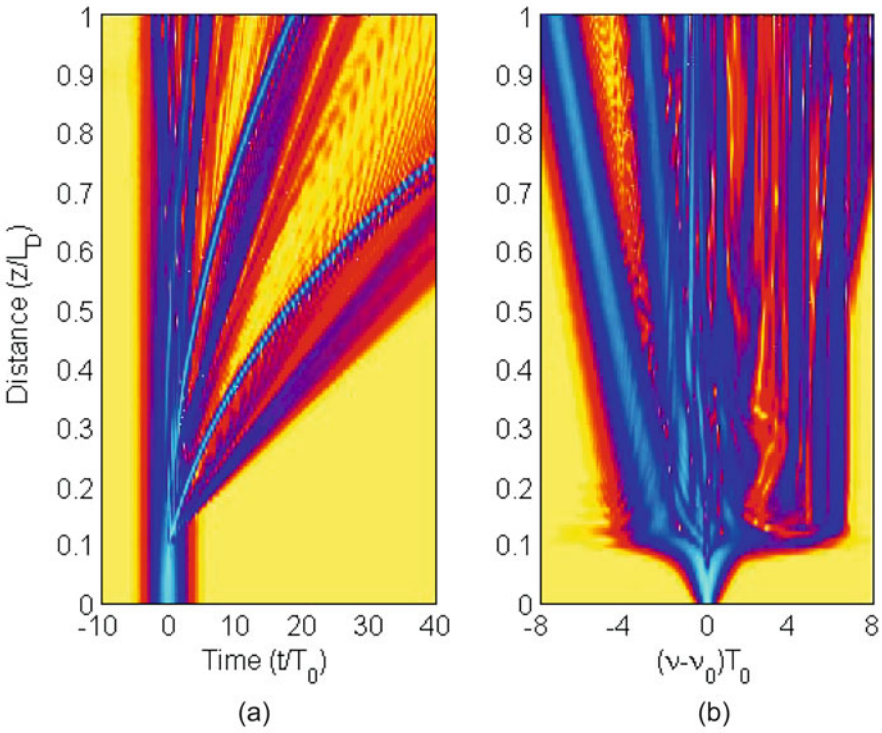

Fig. 3.15 Evolution of an $N = 8$ soliton from $\xi = 0$ to 1 using the parameter values given in the text; (**a**) pulse shape and (**b**) spectrum. The supercontinuum nature of the spectrum becomes apparent for such large values of N. The color scheme is identical to Fig. 3.9

parameters were chosen to be $\delta_3 = 0.02$ and $\delta_4 = 1 \times 10^{-4}$. It is clear from Fig. 3.15 that the pulse evolution becomes quite complex for an $N = 8$ soliton. In particular, the pulse spectrum begins to look like a supercontinuum that extends over a bandwidth that is more than 20 times larger compared to that of the input pulse.

To understand the role of self-steepening, Fig. 3.16 shows the pulse evolution under conditions identical to those used for Fig. 3.15 except that self-steepening is included assuming an input wavelength of 1550 nm; $f_s = 0.0163$ at this wavelength. Clearly, self-steepening affects both the temporal and spectral features. Although it reduces the total width of the supercontinuum, it also makes the supercontinuum more uniform compared to the one in Fig. 3.15. Figure 3.17 compares the input and output pulse spectra for the $N = 8$ soliton after one dispersion length.

Figure 3.16 shows how the pulse spectrum begins to broaden after the fission of an $N = 8$ soliton and how the pulse spreads rapidly in the time domain. However, it does not reveal which parts of the spectrum belong to which parts of the pulse. The mathematical tool for revealing this information is known as the short-time or

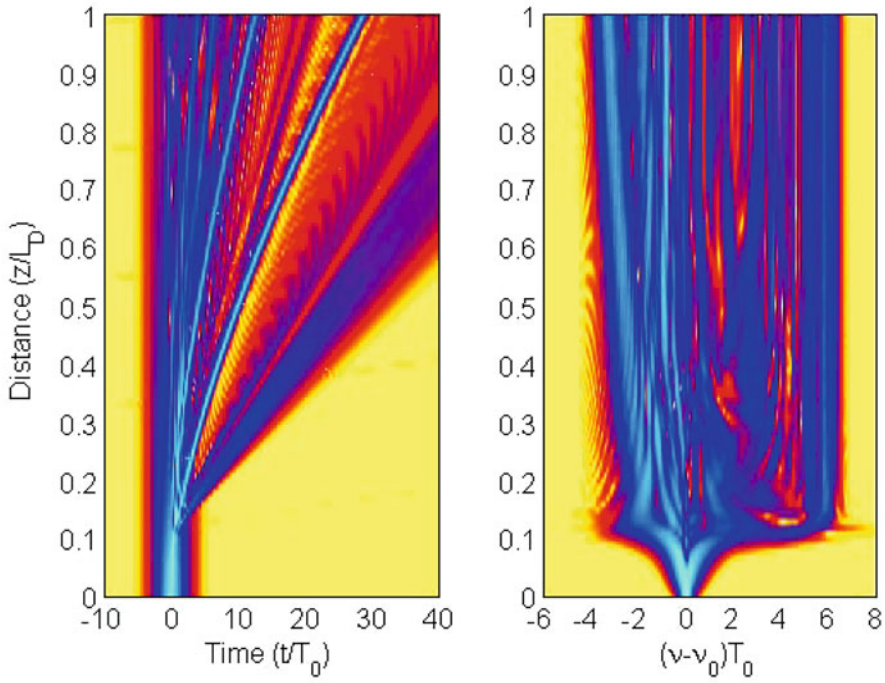

Fig. 3.16 Evolution of an $N = 8$ soliton from $\xi = 0$ to 1 under conditions identical to those used for Fig. 3.15 except that self-steepening is also included. The color scheme is identical to Fig. 3.9

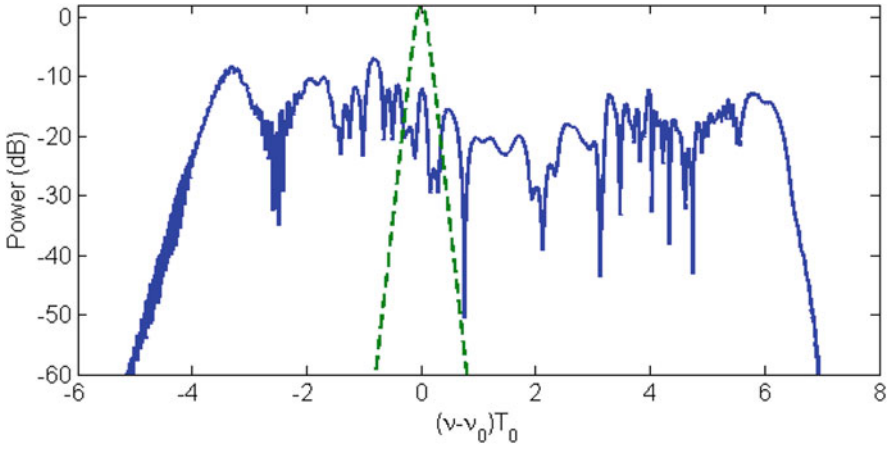

Fig. 3.17 Supercontinuum generated by launching an $N = 8$ soliton into a fiber of length $L = L_D$. The input spectrum is shown for comparison by a dashed green line

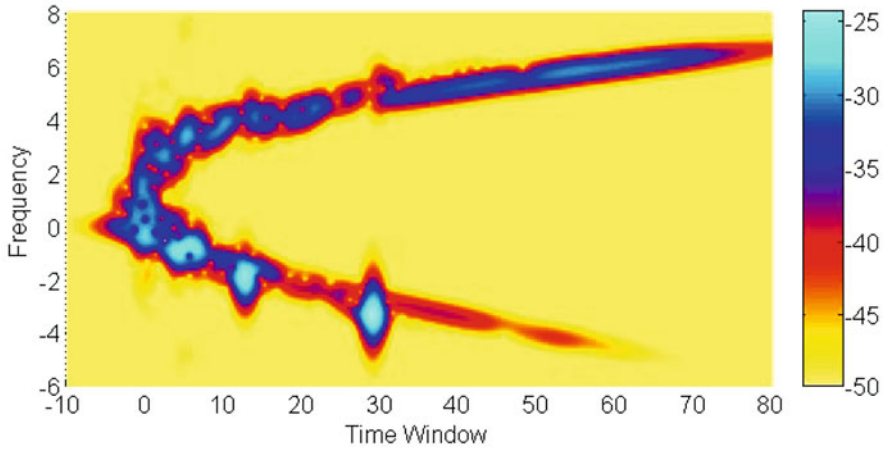

Fig. 3.18 Spectrogram generated numerically at a distance $L = L_D$ by launching an $N = 8$ soliton in a fiber with $L = L_D$. The input spectrum is also shown for comparison by a dashed line

windowed Fourier transform (WFT). In contrast with the optical spectrum, shown in Fig. 3.17 and obtained by taking the Fourier transform of $U(L, \tau)$ over the entire range of τ, the WFT employs a window function that selects $U(L, \tau)$ over a limited range of τ centered at a specific location T. Mathematically, the WFT is given by

$$S(T, \omega) = \left| \int_{-\infty}^{\infty} U(L, \tau) W(\tau - T) \exp(i\omega\tau)\, d\tau \right|^2, \tag{3.30}$$

where $W(\tau - T)$ is the window function centered at $\tau = T$. A Gaussian form is often used for the window function by choosing

$$W(\tau - T) = \frac{1}{\sqrt{2\pi}\sigma} \exp\left[-\frac{(\tau - T)^2}{2\sigma^2} \right], \tag{3.31}$$

where σ controls the window size. The WFT depends on both time and frequency and reveals which parts of the pulse contain which spectral contents. It is also called the spectrogram, a term borrowed from acoustics.

Figure 3.18 shows the spectrogram corresponding to the spectrum shown in Fig. 3.17 by choosing $\sigma = 1$. It shows the output at a distance of one dispersion length when an $N = 8$ soliton is launched into a fiber. The spectral features near $T = 0$ represent SPM-induced spectral broadening of the pulse before it undergoes soliton fission. Two bright spots near $T = 12$ and 28 represent two shortest solitons created after the fission. Their spectra are shifted toward the red side because of intrapulse Raman scattering, the shortest soliton undergoing the most red shift. The two blue-shifted cigar-like features extending over $T = 30$–75 belong to the dispersive waves created by these solitons. Depending on the dispersive properties

of the fiber, such dispersive waves are sometimes trapped by the red-shifted solitons through XPM if they happen to overlap in time.

Spectrograms can be constructed experimentally (Nishizawa & Goto, 2001) using an extension of the frequency resolved optical gating (FROG), a technique used commonly for measuring the width of ultrashort optical pulses (Trebino, 2002). It is referred to as the X-FROG technique, and it consists of performing cross-correlation of the output pulse with a narrow reference pulse whose peak can be shifted using an adjustable delay line. The two pulses overlap inside a nonlinear crystal that creates a signal through sum-frequency generation. Spectrogram is produced by recording a series of optical spectra at the crystal output with different delays between the two pulses.

3.6.2 Supercontinuum Generation Through Modulation Instability

The use of ultrashort optical pulses is not essential for supercontinuum generation. In a 2003 experiment, 42-ns pulses from a Q-switched Nd:YAG laser were launched into a 2-m-long microstructured fiber (with a random hole pattern) to produce a relatively wide supercontinuum at 10-kW peak-power levels (Town et al., 2003). Somewhat surprisingly, it turned out that even continuous-wave (CW) lasers can produce a supercontinuum at sufficiently high power levels. Indeed, CW lasers were used for this purpose as early as 2003, and, by now, such supercontinuum sources are being used for a variety of applications (Avdokhin et al., 2003; Nicholson et al., 2003; Abeeluck et al., 2004; Travers, 2010).

It should come as no surprise that the phenomenon of modulation instability is behind the CW or quasi-CW supercontinuum generation (Travers, 2010). It is well known that when a CW beam propagates in the anomalous-GVD region of an optical fiber, the phenomenon of modulation instability can create amplitude modulations that manifest spectrally as two sidebands at specific frequencies $\omega_0 \pm \Omega_{\max}$, where ω_0 is the frequency of the CW beam (Agrawal, 2019). The frequency shift $\Omega_{\max}$ depends on the input power P_0 and fiber's dispersion and nonlinear parameters as

$$\Omega_{\max} = \sqrt{\frac{2\gamma P_0}{|\beta_2|}}. \tag{3.32}$$

In the case of spontaneous modulation instability, the growth of these sidebands is initiated by intensity fluctuations within the CW beam. Their amplitudes grow initially with distance z exponentially. This growth manifests in the time domain as sinusoidal oscillations with the period $T_m = 2\pi/\Omega_{\max}$. The exponential growth continues as long as the fraction of the power in the two sidebands remains a small fraction of the total power (the so-called linear regime).

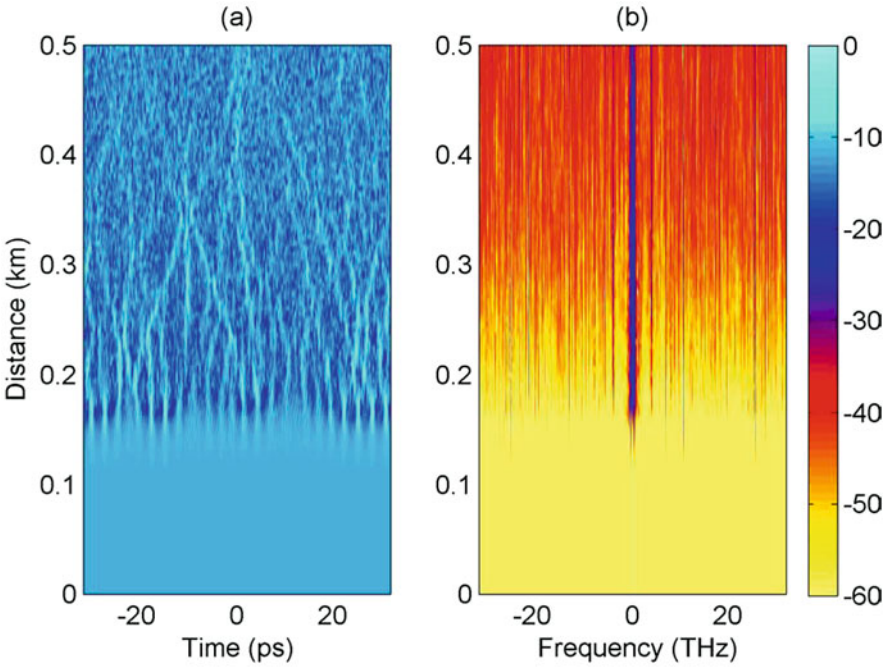

Fig. 3.19 Temporal and spectral evolutions of a noisy CW beam in the anomalous-GVD region of a fiber using parameter values given in the text

Once the modulation-instability process enters the nonlinear regime, evolution of the optical field can only be studied by solving the NLS equation (3.7) numerically with noise added to the input CW beam. Figure 3.19 shows, as an example, the temporal and spectral evolutions of a noisy CW beam assuming $\alpha = 0$, $\beta_2 = -20$ ps^2/km, and $L_{NL} = 10$ m. The TOD is included using $\beta_3 = 0.2$ ps^3/km, but intrapulse Raman scattering is not included in these simulations. The input spectrum is quite narrow in this case and nothing much happens until the onset of modulation instability begins to create spectral sidebands at a frequency predicted by Eq. (3.32), together with the corresponding temporal modulations on the CW beam. Both of these features are clearly apparent in Fig. 3.19 at a distance of about 150 m. With further propagation, temporal modulations become sharper and take the form of a train of short optical pulses of different widths and peak powers that propagate as fundamental solitons in the anomalous-GVD regime of the fiber. The reason why solitons have different widths is related to the noisy nature of spontaneous modulation instability. Indeed, when modulation instability is induced by launching a weak signal at the sideband frequency, all solitons within the pulse train are expected to have nearly the same width.

Even without the Raman effects, one can see supercontinuum formation as more and more spectral sidebands are created through FWM. In the presence of intrapulse

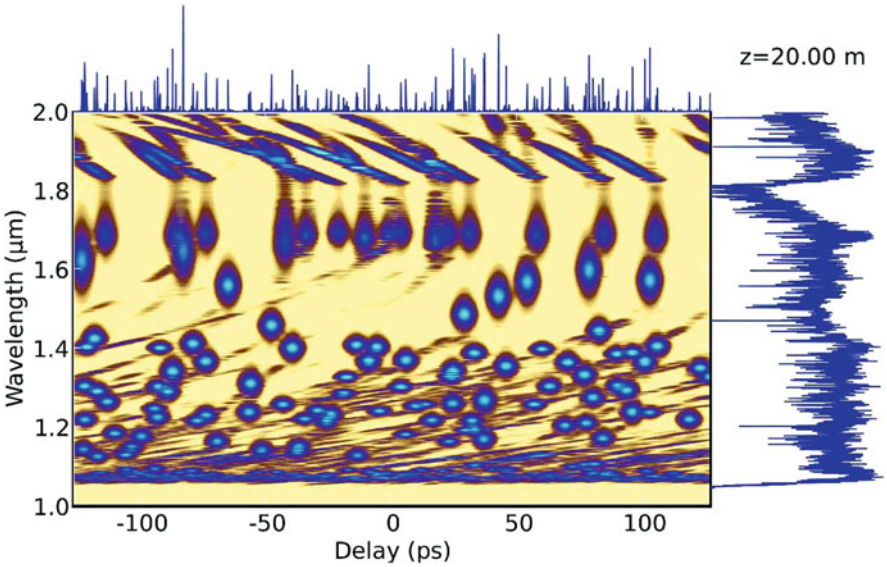

Fig. 3.20 X-FROG spectrogram calculated numerically when a CW beam with 44 W power is launched inside a 20-m-long PCF at a wavelength of 10570 nm. The output pulse train and spectrum are shown on the top and the right side, respectively (After Cumberland et al. (2008); ©2008 OSA.)

Raman scattering, the formation of a supercontinuum proceeds as follows. First, modulation instability converts the CW beam into a train of pulses of different widths and peak powers that propagate as fundamental solitons. Since the RIFS depends on the pulse width, different solitons shift their spectra by different amounts toward longer wavelengths. At the same time, blue-shifted radiation is generated in the form of dispersive waves because of perturbations of these solitons by third-order dispersion. As a soliton shifts its spectrum, it also slows down as long as it experiences anomalous GVD. As a result, solitons collide (overlap temporally) with neighboring solitons and dispersive waves and interact with them though XPM and FWM. It turns out that such a collision can transfer energy to the slowing soliton, which reduces its width further (to maintain the condition $N = 1$) and slows down even more, and its spectrum shifts even further toward longer wavelengths. Multiple soliton collisions eventually produce a supercontinuum that is extended mostly toward the red side of the input wavelength.

Figure 3.20 shows the numerically computed WFT spectrogram of a supercontinuum with parameters corresponding to a 2008 experiment in which a CW beam with 44 W power was launched inside a 20-m-long PCF ($\gamma = 43$ W^{-1}/km) at a wavelength of 1057 nm (Cumberland et al., 2008). The PCF exhibited two ZDWLs located near 810 and 1730 nm. As a result, dispersion was relatively large (65 ps/km/nm) at the pump wavelength of 1070 nm, but it decreased for longer wavelengths. One sees clearly the formation of solitons (round objects)

through modulation instability, together with their different spectral shifts and different speeds (leading to different delays). Collisions among these solitons are also apparent from their temporal overlap. Eventually, the spectrum of a short soliton approaches the ZDWL near 1730 nm, where it stops shifting because of the radiation pressure induced by the corresponding dispersive waves (cigar-like objects) emitted at wavelengths longer than 1730 nm. The interaction (collision) of solitons with these dispersive waves generates new spectral components through FWM in the wavelength region near 1900 nm. The spectrogram in Fig. 3.20 shows both the calculated spectrum and noisy pulse train in the time domain.

It is clear from the preceding description that the noisy nature of the input CW beam plays a critical role since it seeds the process of modulation instability. Even a CW laser beam is only partially coherent because of its finite spectral width resulting from intrinsic phase fluctuations. Any numerical modeling must include such fluctuations. The nonlinear propagation of a partially coherent CW beam inside single-mode optical fibers was investigated in several studies, revealing the physics behind CW supercontinuum generation (Mussot et al. 2004; Vanholsbeeck et al. 2005; Kobtsev & Smirnov, 2005; Cumberland et al. 2008).

The two most important ingredients for generating a CW supercontinuum are a high-power laser and a highly nonlinear fiber so that the product $\gamma P_0 L$ exceeds 30, where P_0 is the CW power launched into a fiber of length L. This condition can be satisfied for a 100-m-long fiber with $\gamma = 100\ \mathrm{W}^{-1}/\mathrm{km}$ at a pump–power level of a few watts. Such power levels are readily available from modern, high-power, Yb-doped fiber lasers. In the original 2003 experiment, a 100-m-long holey fiber was employed, and a Yb-fiber laser was used for CW pumping at 1065 nm (Avdokhin et al., 2003). The resulting supercontinuum extended from 1050 to 1380 nm when 8.7 W of CW power was coupled into the fiber. In a 2004 experiment, highly nonlinear fibers of lengths $\sim$ 1 km were used for supercontinuum generation by launching a CW beam at 1486 nm (Abeeluck et al., 2004). The ZDWL of the fibers was below 1480 nm, resulting in the anomalous GVD at the pump wavelength. Output spectra extended from 1200 to >1800 nm when pump power was close to 4 W. The spectrum was highly asymmetric with much more power on the long-wavelength side. This asymmetry was due to intrapulse Raman scattering that selectively extended the spectrum toward the long-wavelength side. The PCF used in a 2008 experiment exhibited two ZDWLs located near 810 and 1730 nm (Cumberland et al., 2008). When 44 W of CW power was launched into this fiber, the supercontinuum extended from 1050 to 1680 nm. More importantly, the output power was close to 29 W, and the spectral power density exceeded 50 mW/nm up to 1400 nm. These features are useful for applications of such a supercontinuum source for biomedical imaging.

The formation of CW supercontinuum in the visible region has also attracted attention (Cumberland et al., 2008a; Kudlinski et al., 2009, 2010). This is not easy to do because the most practical source of CW radiation is a high-power Yb-fiber laser emitting light near 1060 nm. When such a laser is used with a suitable PCF having its ZDWL near 1000 nm, the observed supercontinuum rarely extends below 900 nm. In a 2006 experiment, a tapered PCF whose core diameter decreased

along its length was employed for this purpose together with a quasi-CW source (a Nd:YAG microchip laser) emitting nanosecond pulse (Kudlinski et al., 2006). The observed supercontinuum extended from 350 to 1750 nm with a high spectral density when the taper length exceeded 5 m. The extension of the supercontinuum into the visible region was possible because of a monotonically decreasing $|\beta_2(z)|$ that allowed the FWM phase-matching condition to be satisfied for progressively shorter idler wavelengths.

In a 2009 experiment, the use of a PCF whose core was both tapered and doped with GeO_2 created a CW supercontinuum that extended toward wavelengths as short as 450 nm (Kudlinski et al., 2009). In the case of a uniform-core PCF pumped at 1075 nm with 70 W of CW power, the supercontinuum extended on the visible side only up to 550 nm and contained no light in the blue region. However, when a uniform-core section of 50 m was followed with a 130-m-long PCF section whose outer diameter decreased from 135 to 85 μm, the supercontinuum extended from 470 to >1750 nm when pumped with 40 W of CW power and thus covered the entire visible region. These results clearly show that an ultrabroad supercontinuum covering both the visible and near-infrared regions can be produced with 1060-nm pumping provided the PCF is suitably designed.

3.6.3 Supercontinuum Pumping in the Normal-GVD Region

From a practical perspective, coherence properties of a supercontinuum are important when it is employed as a broadband source of light for medical, metrological, or other applications. When optical pulses propagate inside a single-mode fiber with a fixed spatial profile, the output is clearly spatially coherent. However, its temporal coherence is affected by fluctuations in the energy, width, and arrival time of individual input pulses. As a result, spectral phase is also likely to fluctuate from pulse to pulse across the bandwidth of the supercontinuum (Dudley et al., 2006). Indeed, coherence measurements show that the spectral coherence of a supercontinuum is limited in practice when the process of soliton fission or modulation instability initiates its buildup (Kobtsev & Smirnov, 2006; Türke et al. 2007; Genty et al. 2010).

The origin of coherence degradation in both cases is related to a noisy process that is very sensitive to small variations in the widths and peak powers associated with the input pulses. It follows that the supercontinuum coherence should improve dramatically if input pulses are launched in the normal-GVD regime of a fiber where solitons cannot form. Indeed, this feature was predicted as early as 2005 in a PCF exhibiting two ZDWLs that was tapered along its length to ensure that optical pulses always experienced normal dispersion (Falk et al., 2005). However, the resulting supercontinuum was not very broad, and its bandwidth was limited to below 400 nm. The problem was solved by 2011, and broadband supercontinua were generated with normal-GVD pumping by using PCFs whose dispersion was suitably tailored (Heidt et al., 2011a; Hooper et al., 2011a; Heidt et al., 2011b).

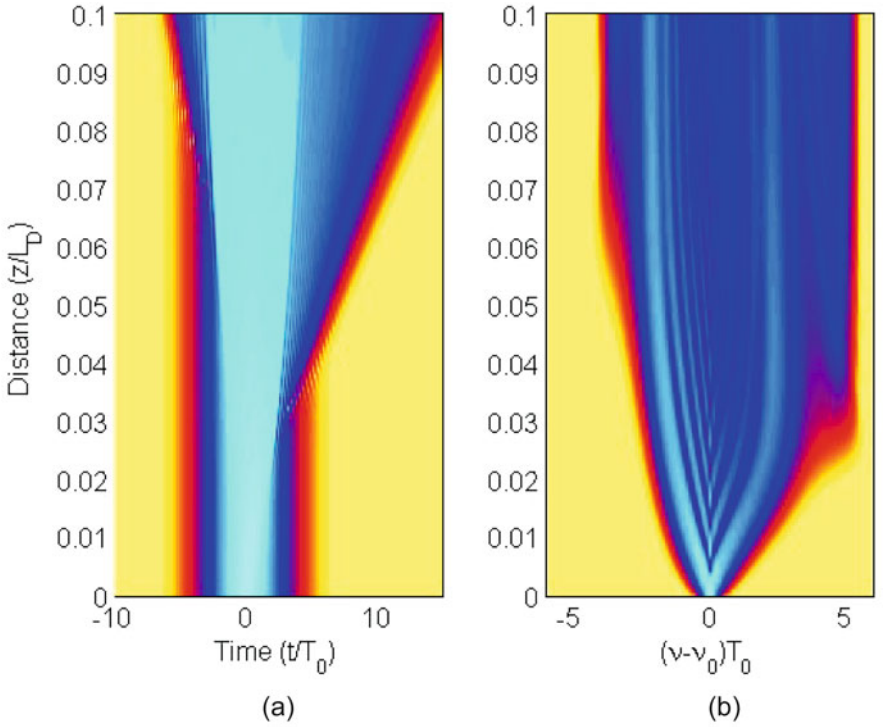

Fig. 3.21 Evolution of (**a**) pulse shape and (**b**) spectrum from $\xi = 0$ to 0.1 in the normal-GVD region when a sech-shape pulse is launched with $N = 30$

As an example, Fig. 3.21 shows the temporal and spectral evolutions of an intense sech-shape pulse launched in the normal-GVD region of a fiber with $N = 30$. The generalized NLS equation (3.4) was solved numerically with $s = 1$, $\delta_3 = 0$, and $\delta_4 = 0.001$ to ensure that the minimum dispersion occurs at the input wavelength of the pulse. It should be compared with Fig. 3.10, obtained for the same input pulse without including the higher-order nonlinear and dispersive effects. In both cases, the spectrum broadens mainly through the SPM but becomes asymmetric in the general case because of self-steepening and intrapulse Raman scattering. Two spectral sidebands are still generated because of optical wave breaking but their amplitudes are quite different. The supercontinuum formed at $z = 0.1L_D$ is relatively uniform over its entire bandwidth. Since soliton fission does not occur, it is also expected to be relatively coherent.

Experiments support the preceding numerical scenario. In a 2011 experiment, the PCF employed was designed such that it exhibited normal GVD over a wavelength region that extended from 400 to beyond 1500 nm (Heidt et al., 2011a). Figure 3.22a shows the broadband spectra observed at the output of a 50-cm-long PCF (fabricated with a 2.3 μm-diameter core) when it was pumped at 1050 nm with 50-fs pulses of

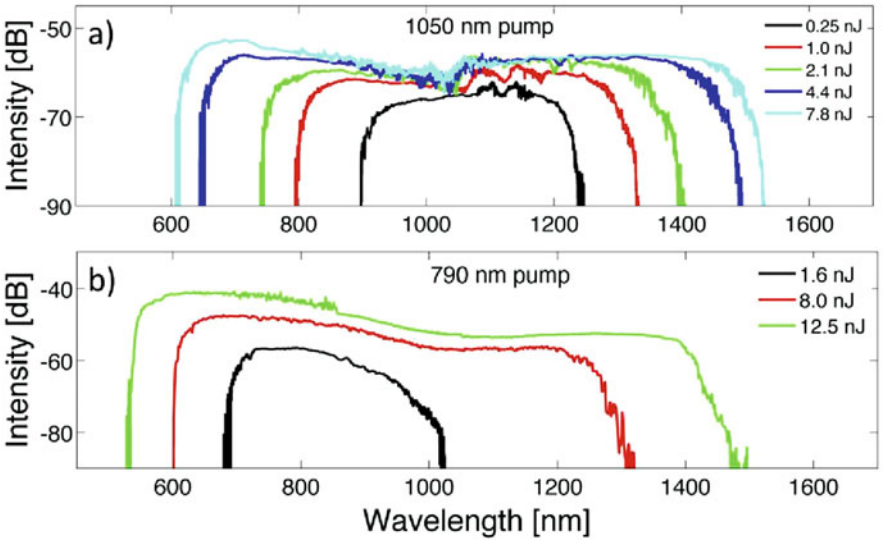

Fig. 3.22 (**a**) Optical spectra observed at the output of a 50-cm-long PCF when it was pumped at a wavelength of 1050 nm with 50-fs pulses of energies ranging from 0.25 to 7.8 nJ. (**b**) Output spectra when the same PCF was pumped at 790 nm (After Heidt et al. (2011a); ©2011 OSA.)

energies ranging from 0.25 to 7.8 nJ. Figure 3.22b shows the output spectra when the same PCF was pumped at 790 nm. In both cases, the supercontinua extend over an 800-nm bandwidth at the highest pulse energy and are relatively flat and smooth compared to those formed in the anomalous-GVD region.

A similar PCF design was used in another 2011 study (Hooper et al., 2011a). It exhibited normal dispersion over a wide wavelength region with a minimum occurring near 1064 nm, the wavelength at which 400-fs input pulses were launched. The output spectrum at the end of a 4-cm-long piece of such a fiber exhibited a shape that is typical of SPM (see Fig. 3.23). When fiber was 1 m long, the supercontinuum extended over 800 nm, and its shape was relatively flat and smooth. Moreover, the output was compressible to a duration of 26 fs and exhibited a high degree of coherence between its spectral components. The width of the compressed pulse was only 5 fs in another experiment (Heidt et al., 2011b) in which octave-spanning spectra were generated by launching 15-fs pulses with 1.7 nJ energy into a fiber that was only 1.7 mm long. Such a coherent supercontinuum is useful for a variety of applications including biomedical imaging. Chapter 6 by Heidt et al. describes in detail supercontinuum generation in the normal-GVD region of an optical fiber.

3.7 Mid-Infrared and Ultraviolet Regions

The experimental results seen in Fig. 3.22 clearly show that the nonlinear effects inside optical fibers can provide a coherent, wideband source of radiation covering the visible and near-infrared regions. An important question is whether a supercontinuum can be extended into the ultraviolet (UV) and mid-infrared (mid-IR) regions because such sources are useful for many practical applications. In this section, we focus first on the mid-IR region and then consider generation of UV radiation.

3.7.1 Supercontinuum in the Mid-Infrared Region

As early as 2000, experiments showed that the supercontinuum extended into the near-IR region up to 1600 nm when a PCF was pumped with short optical pulses at a wavelength near 800 nm (Ranka et al., 2000). Wavelengths beyond 1600 nm could be produced by pumping silica fibers at a wavelength near 1550 nm, but high losses of such fibers in the mid-IR region limited the use of such fibers. A fiber made with lead-silicate glass was used in a 2006 experiment, and it was found that the supercontinuum extended beyond 3 μm, even for a fiber that was only 6 mm long (Omenetto et al., 2006).

As coherent sources in the mid-IR region (wavelength range 3–10 μm) have many applications, the use of nonlinear fibers for producing such radiation became an important area of research after the year 2005. In a 2006 experiment, the supercontinuum was extended to 4500 nm by combining a silica fiber (length ∼1 m) with a few-meter-long fluoride fiber (Xia et al., 2006). Longer wavelengths could not be produced in this experiment because of strong absorption exhibited by fluoride fibers at wavelengths beyond 4500 nm. An ultrabroad supercontinuum was realized in 2009 when a 2-cm-long fluoride fiber was pumped with 180-fs pulses at a wavelength of 1450 nm (Qin et al., 2009). Figure 3.23a shows the output spectrum observed for pulses with 50 MW peak power; its 10 dB bandwidth extends from 565 to 5240 nm. The spectra in the mid-IR region are compared in part (b) for two fibers of different lengths. As seen there, almost the same bandwidth is obtained for the shorter 0.9-cm-long fiber. The drop in power at wavelengths beyond 5 μm is due to high losses of fluoride fibers. In a 2020 experiment (Li et al., 2020), a 60-cm-long fluorotellurite fiber generated a supercontinuum extending from 0.93 to 3.95 μm with a total power of 22.7 W and a high conversion efficiency of 57%.

Starting in 2010, chalcogenide fibers were used to extend the supercontinuum into the mid-IR region (Hudson et al., 2011; Rudy et al., 2013; Yu et al., 2015; Cheng et al., 2016; Karim et al., 2015, 2018; Lemière et al., 2019; Jiao et al., 2019; Yuan et al., 2020). Such fibers have low losses for wavelengths beyond 10 μm and can be made to provide large values of the nonlinear parameter γ. In a 2011 experiment, an As_2S_3 fiber was tapered such that its effective mode area was $< 1\ \mu m^2$, resulting in $\gamma = 12,400\ W^{-1}/km$ at the pump wavelength of 1.55 μm. When 250-fs pulses

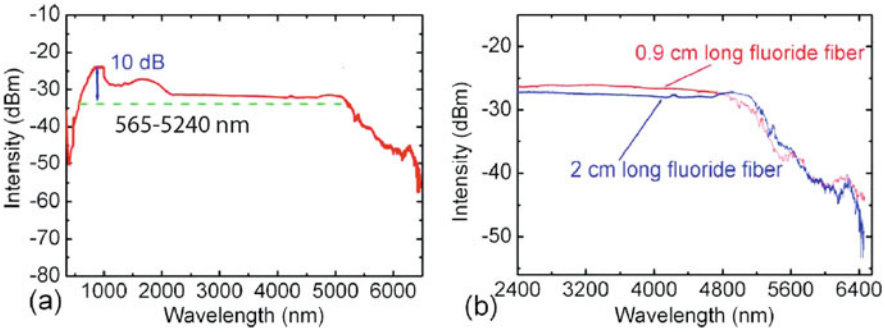

Fig. 3.23 (**a**) Supercontinuum observed at the output of a 2-cm-long fluoride fiber by pumping with 100-fs pulses with a peak power about 50 MW. Dashed line shows the 10-dB bandwidth. (**b**) Comparison of the mid-IR spectra for two fibers of different lengths (After Qin et al. (2009) ©2009 American Institute of Physics.)

were launched into such a 5-cm-long fiber, the supercontinuum extended from 0.97 to near 2 μm (Hudson et al., 2011). A later experiment employed a Tm-doped fiber laser operating at 2.04 μm to pump a 2.1-mm-long As_2S_3 fiber (Rudy et al., 2013). The resulting supercontinuum extended from 1 to 3.7 μm, clearly showing the potential of chalcogenide fibers for mid-IR generation.

This potential was realized in a 2015 experiment that pumped a 11-cm-long fiber with 330-fs pulses at a wavelength of 4.0 μm (Yu et al., 2015). The spectrum extended from 1.8 to 10 μm at the 40-mW average power, and this range was limited by fiber's losses. In a 2016 experiment, losses were reduced enough that the observed supercontinuum extended from 2 to 15 μm, when a 3-cm-long fiber was pumped with 170-fs pulses at a wavelength of 9.8 μm (Cheng et al., 2016). Figure 3.24 shows the measured and stimulated spectra for input pulses with 2.9 MW peak powers. A similar spectral range was realized by using chalcogenide fibers that avoided the use of toxic materials such as arsenic and antimony (Lemière et al., 2019). By 2020, a 16-cm-long microstructured chalcogenide fiber generated a coherent supercontinuum that extended from 2 to 13 μm, when pumped in the normal-GVD region of the fiber with 150-fs pulses at a wavelength of 5 μm (Yuan et al., 2020).

Dispersion engineering plays an important role for chalcogenide fibers used for mid-IR generation. In a 2015 study, three fibers with microstrucured air holes were analyzed for optimizing the fiber's design (Karim et al., 2015). Among these, equiangular spiral microstrucured fiber was found to be the most promising candidate for generating an ultrawide supercontinuum in the mid-IR region. In a later study, a triangular-core fiber was designed such that the predicted supercontinuum extended from 2.3 to 17 μm, when pumped with 100-fs pulses of 3-kW peak power at a wavelength of 4 μm (Karim et al., 2018).

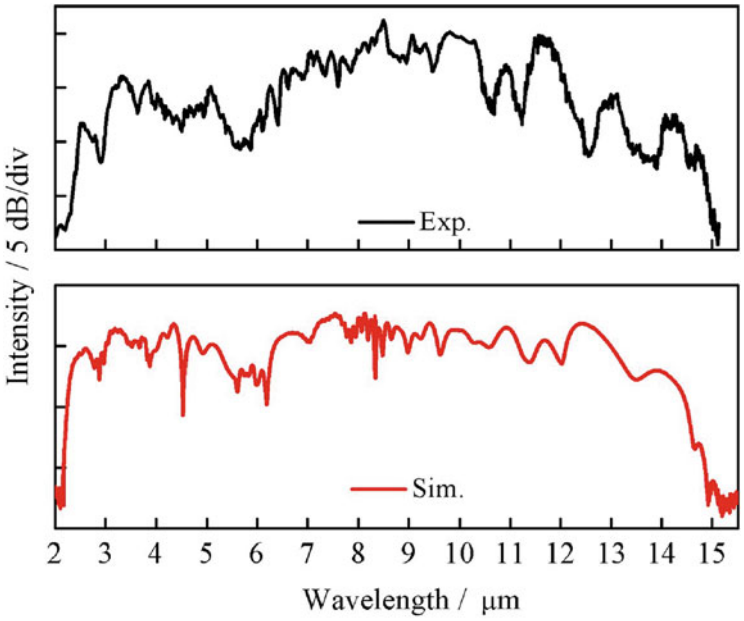

Fig. 3.24 Experimental (top) and simulated (bottom) supercontinuum at the output of a 3-cm-long chalcogenide fiber, pumped at 9.8 μm using 170-fs pulses with 2.9 MW peak power (After Cheng et al. (2016) ©2016 OSA.)

3.7.2 Sources of Ultraviolet Radiation

An important application of the supercontinuum process is to use it as a source of UV radiation. Extending supercontinuum into the UV region is not easy because optical fibers not only become lossy in this region, but their dispersive properties also become unsuitable. The ZDWL of standard silica fibers occurs at a wavelength near 1300 nm such that they provide anomalous GVD at longer wavelengths. The ZDWL can be moved closer to 800 nm by reducing the fiber's core diameter. In fact, the microstructured fiber used for the 2000 supercontinuum experiment (Ranka et al., 2000) had a core diameter close to 2 μm for this reason. For extension into the UV region, the ZDWL must be shifted below 400 nm.

In one approach, the core size of fibers is reduced to below 1 μm, resulting in the so-called nanofibers. As early as 2006, fibers with core diameters ranging from 0.2 to 1.2 μm were made (Gattass et al., 2006). They were used for extending the supercontinuum into the UV region by pumping the tapered fibers with femtosecond pulses at 800 nm. However, the UV radiation near 400 nm was observed only for the fiber with the 1.2-μm core diameter.

In a 2010 experiment, a 5-cm-long tapered PCF, having a core diameter of only 600 nm and exhibiting two ZDWLs at 509 and 640 nm, was employed for extending the supercontinuum into the UV region (Stark et al., 2010). The fiber was pumped

using femtosecond pulses (width <50 fs) whose peak powers could be as high as 4 kW. Input wavelength of 640 nm was near the second ZDWL of the fiber in this experiment. The soliton order N exceeded 200 at peak powers >3 kW. The observed supercontinuum covered the entire visible region and extended into the UV region. It should be noted that the fiber's GVD was anomalous only from 509 to 640 nm, the region between the two ZDWLs. The UV band was formed owing to the dispersive waves emitted by solitons, and it extended as far as 350 nm when the peak power of pulses was close to 4 kW. When the fiber was pumped at 523 nm, the UV band extended from 300 to 470 nm and was intense enough to be useful for practical applications.

It is clear that pumping a fiber at shorter wavelengths will help in producing the UV radiation. An extreme example of this approach was provided in an experiment in which a supercontinuum extending from 350 to 470 nm was produced by pumping a PCF with Q-switched pulses at 355 nm (Sylvestre et al., 2012). The PCF exhibited large normal GVD (β_2 nearly 2000 ps^2/km) and strong absorption in the UV region. It also supported several modes at the pump wavelength (core diameter close to 4 μm). Physical mechanisms behind supercontinuum generation were found to be cascaded SRS and intermodal FWM.

In another study, numerical simulations were used to show that nanofibers with core diameters < 1 μm can extend a supercontinuum into the UV region with pumping in the visible region (Hartung et al., 2012). The fibers were assumed to exhibit normal GVD in both the UV and visible regions. As discussed in Chap. 6, a coherent supercontinuum can be produced under such conditions, without making use of soliton fission or modulation instability. Indeed, the predicted spectra, for a fiber with 450-nm core diameter and pumped at 400 nm with 50-fs pulses, extended into the UV region near 220 nm at a peak power of 80 kW. A similar behavior occurs for suspended-core fibers.

In a different approach, hollow-core fibers are filled with a suitable gas before launching femtosecond pulses into them. In a 2013 study, a 10-cm-long, hollow-core, PCF was filled with different gases and pumped with 38-fs pulses at a wavelength of 805 nm (Mak et al., 2013). The output spectra depended considerably on pulse energy and gas pressure and extended into the UV region near 200 nm because of dispersive waves generated by the perturbed solitons. The same technique was used in a 2020 experiment where an anti-resonant hollow-core fiber was filled with argon gas and pumped with 30-fs pulses obtained from a fiber laser operating at 1030 nm. Figure 3.25 shows how the spectra of dispersive waves emitted in the UV region could be shifted over a range from 220 to 400 nm by varying the pressure of argon gas and the energy of pump pulses (Smith et al., 2020).

It has proved difficult to generate UV wavelengths shorter than 180 nm using gas-filled fibers. In a 2018 study, it was found numerically that wavelengths as short as 90 nm can be realized using a tapered, Ne-filled fiber (Habib et al., 2018). The fiber had a 12-cm-long uniform section that was followed by a 25-cm-long tapered section. It was pumped with 30-fs pulses at 800 nm with peak powers such that each pulse propagated as a fifth-order soliton ($N = 5$) inside the fiber. The higher-order soliton went through a compression phase in the uniform section (down to

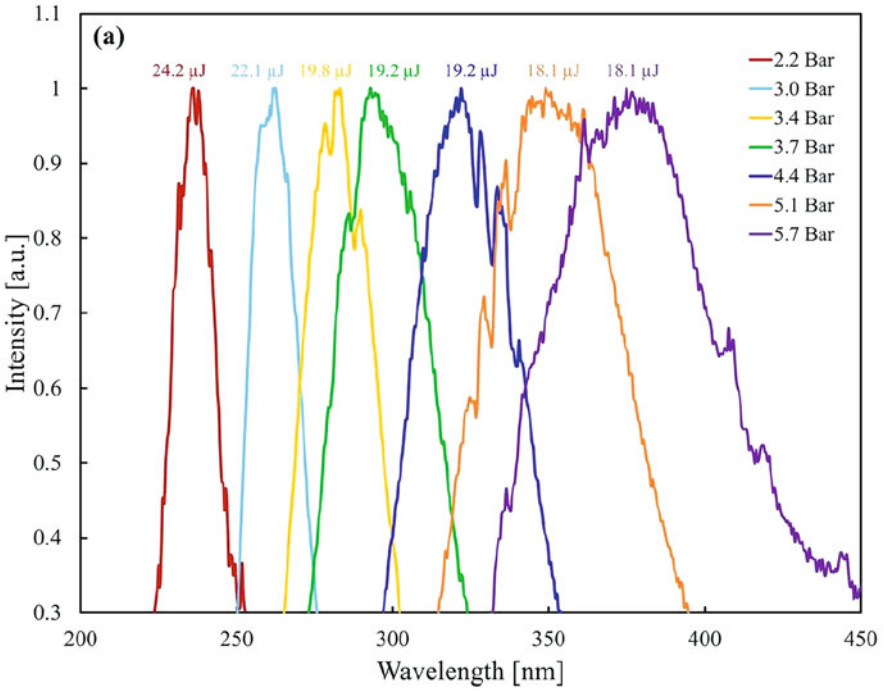

Fig. 3.25 Spectra of dispersive waves in the 220–400 nm range at different pressures of argon gas and energies of 30-fs pump pulses (at 1030 nm) from an argon-filled PCF (After Smith et al. (2020) ©2020 CC BY.)

$<$ 2 fs), which broadened its spectrum and increased its peak power so much that the neon gas was partially ionized. Fission of the compressed fifth-order soliton created multiple dispersive waves whose wavelengths were in the deep UV region. These results indicate that suitably designed, gas-filled fibers provide a practical route for generating the UV radiation.

One may wonder whether it is possible to extend the bandwidth of a supercontinuum so much that it extends from UV to IR regions. Considerable work has been done in recent years to realize such ultrawide spectra. In a 2015 experiment, a 15-cm-long, hollow-core PCF was filled with hydrogen gas. Figure 3.26 shows the ultrawide spectrum obtained when such a fiber was pumped at 805 nm using 30-fs pulses with 2.5-μJ energy (Belli et al., 2015). As seen there, the supercontinuum extended from 120 nm to $>$1000 nm with a relatively strong peak at 182 nm that could be attributed to a dispersive wave. Such a supercontinuum, extending over multiple octaves, is useful for a variety of applications.

It is possible to realize spectra that are even wider than the one in Fig. 3.26. The main issue is related to fiber's losses as it is hard to find a fiber exhibiting low losses over a very wide spectral range. In a 2015 study, a 4-cm-long, zirconium fluoride fiber (known as the ZBLAN fiber) was used because this glass exhibits relatively low

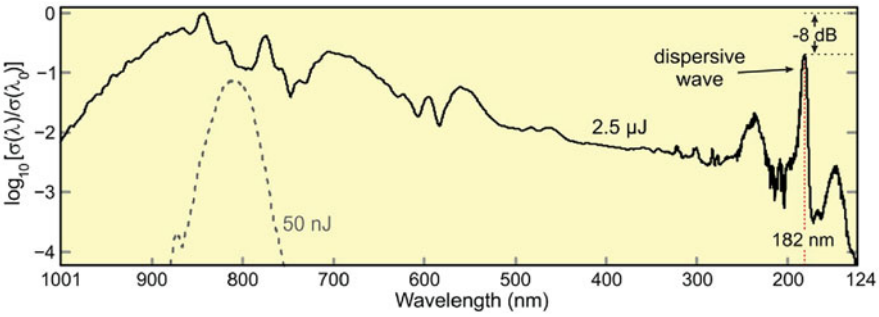

Fig. 3.26 Supercontinuum at the output of a 15-cm-long, H_2-filled, PCF pumped at 805 nm with 30-fs pulses of 2.5-μJ energy. Dashed curves show the low-energy spectrum for comparison (After Belli et al. (2015) ©2015 OSA.)

losses over a wavelength region extending from 0.2 to 6 μm (Jiang et al., 2015). The fiber was in the form of a PCF with a slightly elliptical core (average diameter 3 μm), and its ZDWL was near 1 μm. When it was pumped at a wavelength of 1.04 μm in the anomalous-GVD region with pulse energies of up to 1 nJ, the output spectrum extended from 0.2 to 2.5 μm. In a 2017 experiment, a gas-filled, hollow-core fiber was used containing a single ring of air holes in its cladding (Cassataro et al., 2017). This fiber structure was found to have relatively low losses (<5 dB/m) over a wide spectral range over which its GVD was also relatively flat. The 5-cm-long fiber was filled with the krypton gas at a pressure of 18 bar and pumped with 30-fs pulses of 10 μJ energy at a wavelength of 1.7 μm. Such a pulse formed a 13th-order soliton and produced a supercontinuum that extended from 270 nm to 3100 nm.

Even a wider supercontinuum was obtained in a 2019 experiment using a 30-cm-long, argon-filled, anti-resonant, hollow-core fiber (Adamu et al., 2019). It was realized by pumping the fiber at a wavelength near 2460 nm, where the fiber exhibited an anti-resonant transmission window. When 100-fs pulses with 8-μJ energies were launched into the fiber, the output was in the form of a supercontinuum that extended from 200 nm to 4000 nm. Moreover, the output was spectrally coherent over this entire range. Figure 3.27 shows both the measured ultrawide spectrum (top) and the degree of coherence (bottom). The numerically simulated spectrum is also shown for comparison. The physical mechanism behind the extreme spectral broadening is related to the soliton–plasma nonlinear dynamics that leads to efficient generation of dispersive wave (DW) in the deep UV region. This experiment clearly indicates that the nonlinear effects in suitably designed fibers can produce ultrabroad supercontinua, extending from deep UV to mid-IR regions, with a proper choice of the pump wavelength.

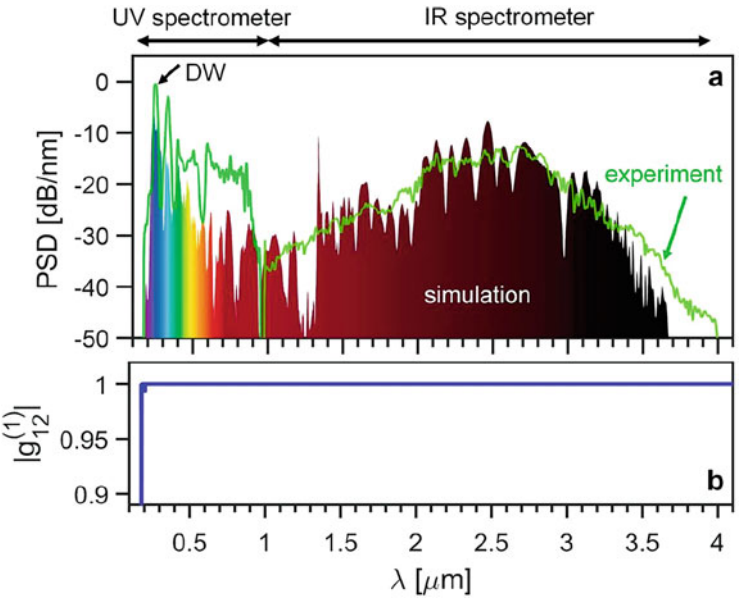

Fig. 3.27 Ultrawide supercontinuum extending from 200 to 4000 nm (top) from an argon-filled, hollow-core fiber pumped at 2460 nm with 100-fs pulses of 8-μJ energy. Simulated spectrum is also shown for comparison. The bottom curve shows measured degree of coherence (After Adamu et al. (2019) ©2019 CC BY.)

3.8 Summary

This chapter has reviewed the propagation characteristics of ultrashort optical pulses in single-mode fibers influenced by various dispersive and nonlinear effects. When pulse widths exceed a few picoseconds and only second-order dispersive effects dominate, the propagation behavior is modeled quite well by the NLS equation. New qualitative features arise depending on whether the propagation occurs in the normal or the anomalous dispersion regime. It is useful to introduce two length scales, L_D and $L_{\rm NL}$, referred to as the dispersion and nonlinear lengths, respectively. A dimensionless parameter defined as $N^2 = L_D/L_{\rm NL}$ plays a particularly important role. The nonlinear effects become important when N is close to or exceeds 1.

In the case of normal GVD, pulses broaden as they propagate and their shape becomes more rectangular. For $N > 10$, the pulse begins to exhibit optical wave breaking and develops a linear chirp across its entire width, a feature that is useful for compressing such pulses. In the case of anomalous GVD, the fiber supports optical solitons that are of fundamental interest and have also found important applications. In this case, the pulse preserves its shape and spectrum throughout its propagation when $N = 1$ and is referred to as the fundamental soliton. In contrast, the pulse evolves in a periodic fashion for other integer values of N.

Much more interesting effects occur for femtosecond pulses, for which one must include both the TOD of the fiber and the phenomenon of intrapulse Raman scattering. Mathematically, one must use a generalized version of the NLS equation. It shows that higher-order solitons undergo a fission process in which an Nth-order soliton is broken into N fundamental solitons of different widths and peak powers. At the same time, dispersive waves are generated through a Cherenkov-like process. For sufficiently large values of N, the onset of dispersive waves in combination with intrapulse Raman scattering, XPM, and FWM leads to the formation of a supercontinuum, whose spectral bandwidth can exceed 1000 nm under suitable conditions. Depending on the input wavelength of the optical pulses and the material used to make the fiber, a supercontinuum can be produced to cover the visible, near-IR, or the mid-IR spectral regions. With a proper choice of the pump wavelength, hollow-core fibers filled with gases can be used to obtain ultrawide supercontinua that extend from deep UV to mid-IR regions and are spectrally coherent over the entire wavelength range.

The use of optical fibers for supercontinuum generation has found a variety of applications, especially in the area of biomedical imaging. Indeed, fiber-based supercontinuum sources have been available commercially for more than a decade by now. Clearly, optical fibers provide an extremely versatile optical medium for studying nonlinear phenomena and for creating novel optical sources in different spectral regions. Such sources are already used and will continue to be used for a variety of applications in diverse areas of optics and photonics.

References

Abeeluck, A. K., Headley, C., & Jørgensen, C. G. (2004). High-power supercontinuum generation in highly nonlinear, dispersion-shifted fibers by use of a continuous-wave Raman fiber laser. *Optics Letters, 29*, 2163–2164.

Adamu, A. I., Habib, M. S., Petersen, C. R., Lopez, J. E. A., Zhou, B., Schülzgen, A., Bache, M., Amezcua-Correa, R., Bang, O., & Markos, C. (2019). Deep-UV to mid-IR supercontinuum generation driven by mid-IR ultrashort pulses in a gas-filled hollow-core fiber. *Scientific Reports, 9*, 4446.

Agrawal, G. P. (2019). *Nonlinear fiber optics* (6th ed.) New York: Academic.

Agrawal, G. P. (2020). *Applications of nonlinear fiber optics* (3rd ed.). New York: Academic.

Alfano, R. R., & Shapiro, S. L. (1970a). Emission in the region 4000 to 7000 Åvia four-photon coupling in glass. *Physical Review Letters, 24*, 584–587.

Alfano, R. R., & Shapiro, S. L. (1970b). Observation of self-phase modulation and small scale filaments in crystals and glasses. *Physical Review Letters, 24*, 592–594.

Alfano, R. R., & Shapiro, S. L. (1970c). Direct distortion of electronic clouds of rare gas atoms in intense electric fields. *Physical Review Letters, 24*, 1217–1220.

Alfano, R. R., & Shapiro, S. L. (1971). Picosecond spectroscopy using the inverse Raman effect. *Chemical Physics Letters, 8*, 631–633.

Akhmediev, N., & Karlsson, M. (1995). Cherenkov radiation emitted by solitons in optical fibers. *Physical Review A, 51*, 2602–2607.

Avdokhin, A. V., Popov, S. V., & Taylor, J. R. (2003). Continuous-wave, high-power, Raman continuum generation in holey fibers. *Optics Letters, 28*, 1353–1355.

Beaud, P., Hodel, W., Zysset, B., & Weber, H. P. (1987). Ultrashort pulse propagation, pulse breakup, and fundamental soliton formation in a single-mode optical fiber. *IEEE Journal of Quantum Electronics, 23*, 1938–1946.

Belli, F., Abdolvand, A., Chang, W., Travers, J. C., & Russell, P. St. J. (2015). Vacuum-ultraviolet to infrared supercontinuum in hydrogen-filled photonic crystal fiber. *Optica, 2*, 292–300.

Cassataro, M., Novoa, D., Günendi, M. C., Edavalath, N. N., Frosz, M. H., Travers, J. C., Russell, P. St. J. (2017). Generation of broadband mid-IR and UV light in gas-filled single-ring hollow-core PCF. *Optics Express, 25*, 7637–7644.

Cheng, T., Nagasaka, K., Tuan, T. H., Xue, X., Matsumoto, M., Tezuka, H., Suzuki, T., & Ohishi, Y. (2016). Mid-infrared supercontinuum generation spanning 2.0 to 15.1 μm in a chalcogenide step-index fiber. *Optics Letters, 41*, 2117–2120.

Cumberland, B. A., Travers, J. C., Popov, S. V., & Taylor, J. R. (2008). 29 W high power CW supercontinuum source. *Optics Express, 16*, 5954–5962.

Cumberland, B. A., Travers, J. C., Popov, S. V., & Taylor, J. R. (2008a). *Optics Letters, 33*, 2122.

J. M. Dudley & J. R. Taylor, (Eds.). (2010). *Supercontinuum generation in optical fibers* Cambridge: Cambridge University Press.

Dudley, J. M., Genty, G., & Coen, S. (2006). Supercontinuum generation in photonic crystal fiber. *Reviews of Modern Physics, 78*, 1135–1184.

Falk, P., Frosz, M. H., & Bang, O. (2005). Supercontinuum generation in a photonic crystal fiber with two zero-dispersion wavelengths tapered to normal dispersion at all wavelengths. *Optics Express, 13*, 7535–7540.

Fork, R. L., Brito Cruz, C. H., Becker, P. C., & Shank, C. V. (1987). Compression of optical pulses to six femtoseconds by using cubic phase compensation. *Optics Letters, 12*, 483–485.

Gattass, R. R., Svacha, G. T., Tong, L., & Mazur, E. (2006). Supercontinuum generation in submicrometer diameter silica fibers. *Optics Express, 14*, 9408–9414.

Genty, G., Coen, S., & Dudley, J. M. (2007). Fiber supercontinuum sources. *Journal of the Optical Society of America, 24*, 1771–1785.

Genty, G., Surakka, M., Turunen, J., & Friberg, A. T. (2010). Second-order coherence of supercontinuum light. *Optics Letters, 35*, 3057–3059.

Gordon, J. P. (1986). Theory of the soliton self-frequency shift. *Optics Letters, 11*, 662–664.

Gordon, J. P. (1992). Dispersive perturbations of solitons of the nonlinear Schrödinger equation. *Journal of the Optical Society of America B, 9*, 91–97.

Habib, M. S., Markos, C., Antonio-Lopez, J. E., Correa, R. A., Bang, O., & Bache, M. (2018). Multi-stage generation of extreme ultraviolet dispersive waves by tapering gas-filled hollow-core anti-resonant fibers. *Optics Express, 26*, 24357.

Hartung, A., Heidt, A. M., & Bartelt, H. (2012). Nanoscale all-normal dispersion optical fibers for coherent supercontinuum generation at ultraviolet wavelengths. *Optics Express, 20*, 13777–13788.

Hasegawa, A., & Tappert, F. (1973). Transmission of stationary nonlinear optical pulses in dispersive dielectric fibers: I. Anomalous dispersion. *Applied Physics Letters, 23*, 142–144.

Heidt, A. M., Hartung, A., Bosman, G. W., Krok, P., Rohwer, E. G., Schwoerer, H., & Bartelt, H. (2011a). Coherent octave spanning near-infrared and visible supercontinuum generation in all-normal dispersion photonic crystal fibers. *Optics Express, 19*, 3775–3787.

Heidt, A. M., Rothhardt, J., Hartung, A., Bartelt, H., Rohwer, E. G., Limpert, J., & Tünnermann, A. (2011b). High quality sub-two cycle pulses from compression of supercontinuum generated in all-normal dispersion photonic crystal fiber. *Optics Express, 19*, 13873–13879.

Hooper, L. E., Mosley, P. J., Muir, A. C., Wadsworth, W. J., & Knight, J. C. (2011a). Coherent supercontinuum generation in photonic crystal fiber with all-normal group velocity dispersion. *Optics Express, 19*, 4902–4907.

Hudson, D. D., Dekker, S. A., Mägi, E. C., Judge, A. C., Jackson, S. D., Li, E., Sanghera, J. S., Shaw, L. B., Aggarwal, I. D., & Eggleton, B. J. (2011). Octave spanning supercontinuum in an As_2S_3 taper using ultralow pump pulse energy. *Optics Letters, 36*, 1122.

Jiang, X., Joly, N. Y., Finger, M. A., Babic, F., Wong, G. K. L., Travers, J. C., & Russell, P. St. J. (2015). Deep-ultraviolet to mid-infrared supercontinuum generated in solid-core ZBLAN photonic crystal fibre. *Nature Photonics, 9*, 133.

Jiao, K., Yao, J., Zhao, Z., Wang, X., Si, N., Wang, X., Chen, P., Xue, Z., Tian, Y., Zhang, B., Zhang, P., Dai, S., Nie, Q., & Wang, R. (2019). Mid-infrared flattened supercontinuum generation in all-normal dispersion tellurium chalcogenide fiber. *Optics Express, 27*, 2036–2043.

Karim, M. R., Rahman, B. M. A., Azabi, Y. O., Agrawal, A., & Agrawal, G. P. (2015). Ultrabroadband mid-infrared supercontinuum generation through dispersion engineering of chalcogenide microstructured fibers. *Journal of the Optical Society of America B, 32*, 2343–2352.

Karim, M. R., Ahmad, H., & Rahman, B. M. A. (2018). Design and modeling of dispersion-engineered all-chalcogenide triangular-core fiber for mid-infrared-region supercontinuum generation. *Journal of the Optical Society of America B, 35*, 266–275.

Kobtsev, S. M., & Smirnov, S. V. (2005). Modelling of high-power supercontinuum generation in highly nonlinear, dispersion shifted fibers at CW pump. *Optics Express, 13*, 6912–8918.

Kobtsev, S. M., & Smirnov, S. V. (2006). Coherent properties of supercontinuum containing clearly defined solitons. *Optics Express, 14*, 3968–3980.

Kodama, Y., & Hasegawa, A. (1987). Nonlinear pulse propagation in a monomode dielectric guide. *IEEE Journal of Quantum Electronics, 23*, 510–524.

Kudlinski, A., George, A. K., Knight, J. C., Travers, J. C., Rulkov, A. B., Popov, S. V., & Taylor, J. R. (2006). Zero-dispersion wavelength decreasing photonic crystal fibers for ultraviolet-extended supercontinuum generation. *Optics Express, 14*, 5715–5722.

Kudlinski, A., Bouwmans, G., Vanvincq, O., Quiquempois, Y., Le Rouge, A., Bigot, L., Mélin, G., & Mussot, A. (2009). White-light CW-pumped supercontinuum generation in highly GeO_2-doped core photonic crystal fibers. *Optics Letters, 34*, 3631–3634.

Kudlinski, A., Barviau, B., Leray, A., Spriet, C., Héliot, L., & Mussot, A. (2010). Control of pulse-to-pulse fluctuations in visible supercontinuum. *Optics Express, 18*, 27445–27454.

Lemière, A., Désévédavy, F., Mathey, P., Froidevaux, P., Gadret, G., Jules, J.-C., Aquilina, C., Kibler, B., Béjot, P., Billard, F., Faucher, O., & Smektala, F. (2019). Mid-infrared supercontinuum generation from 2 to 14 μm in arsenic- and antimony-free chalcogenide glass fibers. *Journal of the Optical Society of America B, 36*, A183–A192.

Li, Z., Jia, Z., Yao, C., Zhao, Z., Li, N., Hu, M., Ohishi, Y., Qin, W., & Qin, G. (2020). 22.7 W mid-infrared supercontinuum generation in fluorotellurite fibers. *Optics Letters, 45*, 1882–1885.

Lin, Q., & Agrawal, G. P. (2006). Raman response function for silica fibers. *Optics Letters, 31*, 3086–3088.

Lin, C., & Stolen, R. H. (1976). New nanosecond continuum for excited-state spectroscopy. *Applied Physics Letters, 28*, 216–228.

Liu, X., Xu, C., Knox, W. H., Chandalia, J. K., Eggleton, B. J., Kosinski, S. G., & Windeler, R. S. (2001). Soliton self-frequency shift in a short tapered air–silica microstructure fiber. *Optics Letters, 26*, 358–360.

Mak, K. F., Travers, J. C., Hölzer, P., Joly, N. Y., & Russell, P. St. J. (2013). Tunable vacuum-UV to visible ultrafast pulse source based on gas-filled Kagome-PCF. *Optics Express, 21*, 10942–10953.

Maker, P. D., Terhune, R. W., & Savage, C. M. (1964). Intensity-dependent changes in the refractive index of liquids. *Physical Review Letters, 12*, 507–509 (1964).

Mitschke, F. M., & Mollenauer, L. F. (1986). Discovery of the soliton self-frequency shift. *Optics Letters, 11*, 659–661.

Mollenauer, L. F., & Stolen, R. H. (1984). The soliton laser. *Optics Letters, 9*, 13–15.

Mollenauer, L. F., Stolen, R. H., & Gordon, J. P. (1980). Experimental observation of picosecond pulse narrowing and solitons in optical fibers. *Physical Review Letters, 45*, 1095–1098.

Mussot, A., Lantz, E., Maillotte, H., Sylvestre, R., Finot, C., & Pitois, S. (2004). Spectral broadening of a partially coherent CW laser beam in single-mode optical fibers. *Optics Express, 12*, 2838–2843.

Nicholson, J. W., Abeeluck, A. K., Headley, C., Yan, M. F., & Jørgensen, C. G. (2003). Pulsed and continuous-wave supercontinuum generation in highly nonlinear, dispersion-shifted fibers. *Applied Physics B, 77*, 211–218.

Nishizawa, N., & Goto, T. (2001). Experimental analysis of ultrashort pulse propagation in optical fibers around zero-dispersion region using cross-correlation frequency resolved optical gating. *Optics Express, 8*, 328–334.

Omenetto, F. G., Wolchover, N. A., Wehner, M. R., Ross, M., Efimov, A., Taylor, A. J., Kumar, V. V. R. K., George, A. K., Knight, J. C., Joly, N. Y., & Russell, P. St. J. (2006). Spectrally smooth supercontinuum from 350 nm to 3 μm in sub-centimeter lengths of soft-glass photonic crystal fibers. *Optics Express, 14*, 4928–4934.

Qin, G., Yan, X., Kito, C., Liao, M., Chaudhari, C., Suzuki, T., & Ohishi, Y. (2009). Ultrabroadband supercontinuum generation from ultraviolet to 6.28 μm in a fluoride fiber. *Applied Physics Letters, 95*, 161103.

Ranka, J. K., Windeler, R. S., & Stentz, A. J. (2000). Visible continuum generation in air–silica microstructure optical fibers with anomalous dispersion at 800 nm. *Optics Letters, 25*, 25–27.

Roy, S., Bhadra, S. K., & Agrawal, G. P. (2009). Dispersive waves emitted by solitons perturbed by third-order dispersion inside optical fibers. *Physical Review A, 79*, 023824.

Rudy, C. W., Marandi, A., Vodopyanov, K. L., & Byer, R. L. (2013). Octave-spanning supercontinuum generation in in situ tapered As_2S_3 fiber pumped by a thulium-doped fiber laser. *Optics Letters, 38*, 2865–2868.

Santhanam, J., & Agrawal, G. P. (2003). Raman-induced spectral shifts in optical fibers: general theory based on the moment method. *Optics Communications, 222*, 413–420.

Smith, C. R., Moltke, A., Adamu, A. I., Michieletto, M., Bowen, P., Moselund, P. M., Markos, C., & Bang, O. (2020). Low-noise tunable deep-ultraviolet supercontinuum laser. *Scientific Reports, 10*, 18447.

Stark, S. P., Podlipensky, A., Joly, N. Y., & Russell, P. St. J. (2010). Ultraviolet-enhanced supercontinuum generation in tapered photonic crystal fiber. *Journal of the Optical Society of America B, 27*, 592–598.

Stolen, R. H. (2008). The early years of fiber nonlinear optics. *Journal of Lightwave Technology, 26*, 1021–1031.

Stolen, R. H., & Lin, C. (1978). Self-phase-modulation in silica optical fibers. *Physical Review A, 17*, 1448–1453.

Stolen, R. H., Gordon, J. P., Tomlinson, W. J., & Haus, H. A. (1989). Raman response function of silica-core fibers. *Journal of the Optical Society of America B, 6*, 1159–1166.

Sylvestre, T., Ragueh, A. R., Lee, M. W., Stiller, B., Fanjoux, G., Barviau, B., Mussot, A., & Kudlinski, A. (2012). Black-light continuum generation in a silica-core photonic crystal fiber. *Optics Letters, 37*, 130–132.

Tomlinson, W. J., Stolen, R. H., & Johnson, A. M. (1985). Optical wave breaking in nonlinear optical fibers. *Optics Letters, 10*, 457–459.

Town, G. E., Funaba, T., Ryan, T., & Lyytikainen, K. (2003). Optical supercontinuum generation from nanosecond pump pulses in an irregularly microstructured air-silica optical fiber. *Applied Physics B, 77*, 235–238.

Travers, J. C. (2010). Continuous wave supercontinuum generation. In J. M. Dudley & J. R. Taylor (Eds.) *Supercontinuum generation in optical fibers* (Chap. 8). Cambridge: Cambridge University Press.

Trebino, R. (2002). *Frequency-resolved optical gating: The measurement of ultrashort laser pulses*. New York: Springer.

Türke, D., Pricking, S., Husakou, A., Teipel, J., Herrmann, J., & Giessen, H. (2007). Coherence of subsequent supercontinuum pulses generated in tapered fibers in the femtosecond regime. *Optics Express, 15*, 2732–2741.

Vanholsbeeck, F., Martin-Lopez, S., González-Herráez, M., & Coen, S. (2005). The role of pump incoherence in continuous-wave supercontinuum generation. *Optics Express, 13*, 6615.

Wai, P. K. A., Menyuk, C. R., Lee, Y. C., & Chen, H. H. (1986). Nonlinear pulse propagation in the neighborhood of the zero-dispersion wavelength of monomode optical fibers. *Optics Letters, 11*, 464–488.

Wai, P. K. A., Chen, H. H., & Lee, Y. C. (1990). Radiations by solitons at the zero group-dispersion wavelength of single-mode optical fibers. *Physical Review A, 41*, 426–439.

Xia, C., Kumar, M., Kulkarni, O. P., Islam, M. N., Terry, F. L., Freeman, M. J., Poulain, M., & Mazé, G. (2006). Mid-infrared supercontinuum generation to 4.5 μm in ZBLAN fluoride fibers by nanosecond diode pumping. *Optics Letters, 31*, 2553–2556.

Yu, Y., Zhang, B., Gai, X., Zhai, C., Qi, S., Guo, W., Yang, Z., Wang, R., Choi, D.-Y., Madden, S., & Luther-Davies, B. (2015). 1.8–10 μm mid-infrared supercontinuum generated in a step-index chalcogenide fiber using low peak pump power. *Optics Letters, 40*, 1081–1084.

Yuan, Y., Yang, P., Peng, X., Cao, Z., Ding, S., Zhang, N., Liu, Z., Zhang, P.G., Wang, X., & Dai, S. (2020). Ultrabroadband and coherent mid-infrared supercontinuum generation in all-normal dispersion Te-based chalcogenide all-solid microstructured fiber. *Journal of the Optical Society of America B, 37*, 227–232.